Russian Chemical Reviews **80** (4) 293 – 312 (2011) © 2011 Russian Academy of Sciences and Turpion Ltd

DOI 10.1070/RC2011v080n04ABEH004163

X-Ray diffraction structure diagnostics of nanomaterials

E M Moroz

Contents

I.	Introduction	293
II.	X-Ray diffraction method of investigation of the radial distribution of electrons: general	294
III.	Comparative method of the radial electron density distribution	298
IV.	Investigations of oxide supports for catalysts	301
V.	Conclusion	310

Abstract. The review concerns the development and applications of the X-ray diffraction method of the radial electron density distribution based on the integral analysis of X-ray diffraction in studies of nanomaterials, in particular, oxide supports for catalysts. The method provides information on the interatomic distances and coordination numbers in the structure and allows one to detect and estimate the size of nanostructures (phases) less than 3 nm in size, which cannot be detected by conventional powder X-ray diffraction analysis. The method is sensitive to the changes in the local structure measuring 1 – 3 unit cells; therefore, it is successfully used to identify various defects in nanoobjects of any chemical composition. The bibliography includes 124 references.

I. Introduction

The state-of-the-art in the field of design of efficient nanomaterials is determined not only by the development of novel methods for their synthesis and correct testing of the physicochemical properties, but also by the level of structure diagnostics because the structure of nanocrystalline phases is an important characteristic which determines the properties of nanomaterials. A key issue in certification of nanomaterials is the identification of the composition and structural features of constituent phases. For instance, in the case of supported metal catalysts (typical representatives of nanomaterials), the local structure of catalytically active metal nanoparticles and clusters is usually different from the structure of the bulk metallic phase owing to, *e.g.*, the interaction with the support matrix. This striking example shows that structure diagnostics of catalysts requires methods that take into account the specific features of the local structure of their components.

Information on the phase composition and structure of a material is most often obtained by X-ray diffraction techniques based on analysis of positions, profiles and intensities of Bragg reflections. Information on the averaged atomic structure and the parameters determining the substructural characteristics of a material is obtained using various kinds of full-profile analysis (FPA), based on consideration of an array of diffraction peaks, and by studying the substructural characteristics using a harmonic analysis of the profiles of particular peaks. However, there are some reasons why these methods are often difficult-to-use and low-informative in the structural studies of nanomaterials.

First, a characteristic feature of nanomaterials is high dispersion and disorder of the constituent phases; therefore, their diffraction patterns are characterized by significant broadening of peaks up to merging with the background.

Second, structural studies of nanocomposites are complicated by the problem of determination of quantitative relations between phases [*e.g.*, the catalytically active metal nanoparticles and particles of the matrix (support) in the case of supported catalysts]. Often, researchers work with highly dilute systems. In this situation, the contribution of the highly disperse active component to the diffraction pattern is very small, which complicates its analysis.

Third, diffraction from a nanocomposite system may be nonadditive owing to the interactions between constituent nanophases.

Fourth, nanocrystalline materials are often characterized by high defectiveness, local distortions of the periodic structure and by the existence of interblock boundaries. These features favour production of additional strain that distorts the structure of crystallites.

The factors mentioned above cause changes in the diffraction pattern. At the same time, nanophases are often stabilized just due to structural defects or the interaction with the matrix on which they are formed. Owing to this, the averaged structure of nanophases differs from the local structure, although the latter often determines such

E M Moroz G K Boreskov Institute of Catalysis, Siberian Branch of the Russian Academy of Sciences, prosp. Akad. Lavrentieva 5, 630090 Novosibirsk, Russian Federation. Fax (7-383) 330 80 56, tel. (7-383) 326 95 32, e-mail: emoroz@catalysis.ru

Received 1 June 2010
Uspekhi Khimii **80** (4) 315 – 334 (2011); translated by A M Raevskiy

important properties of nanostructures as the thermal stability, mechanical strength, electronic, optical, catalytic properties, *etc*.

From the aforesaid it is clear that the progress in studies of the phase composition and peculiarities of the local structure of nanosystems require the development of methods that take into account the specific features of X-ray scattering by such systems. Considerable interest in nanomaterials is stimulated by elaboration of relevant methods for structure diagnostics; therefore, a number of research groups have been developing novel approaches and software for structural analysis of nanocrystals from general considerations concerning X-ray scattering by materials.[1–5]

The largest amount of structural information can be extracted from the full profile of the X-ray diffraction pattern. Therefore, investigations of highly disperse materials require the development of methods which use this information. The diffraction pattern from polycrystals with coherent scattering regions smaller than 1–3 nm is similar to the diffraction pattern from an amorphous material, namely, it is characterized by broad diffuse halos. In this connection, it is appropriate to investigate the structure of nanoobjects by the methods that are used to study X-ray amorphous materials (liquids, glasses, alloys).[6,7] The structure of such materials is studied by an X-ray diffraction method of radial distribution of atoms (RDA) or the radial electron density distribution (REDD),[8–11] also known as analysis of pair distribution functions (PDF analysis). The last-mentioned method has been intensively developed by the Nanoscale Interdisciplinary Research Team (NIRT) on the Structure of Nanocrystals comprising leading university researchers from the USA.[12–16]

Interesting structural information can also be obtained by X-ray absorption fine structure (XAFS) spectroscopy, which allows one to study the fine structure of X-ray spectra near the atomic absorption edges.

By analyzing absorption spectra one can study the electronic structure and the structure of the local environment of the atoms under investigation. For instance, studying the pattern of the near-edge absorption one can determine the symmetry and extent of distortion of the local atomic environment. The X-ray absorption near edge structure (XANES) technique makes it possible to study the fine structure at energies up to 30 eV higher than the absorption edge. This method allows one to determine the valence of atoms, the electron density distribution and the electronic band structure. Extended X-ray absorption fine structure (EXAFS) studies of an extended fine structure spanning a range from 30 to nearly 1500 eV above the absorption edge enable a highly accurate determination of the interatomic distances, coordination numbers and types of atoms in the local environment of the probe atoms. XAFS spectroscopy offers an undoubtful advantage over traditional X-ray methods of investigation for systems of complex chemical composition, especially at relatively low concentrations of the atoms of interest.[17–21]

A considerable advantage of EXAFS over REDD is selectivity, *viz*., EXAFS operates with distances from different atoms to a given atom, whereas the REDD technique involves summation of all specified distances irrespective of the nature of the atom. However, the advantage of the REDD method is that it gives absolute values of the interatomic distances, whereas EXAFS gives the interatomic distances corrected for the phase shift. In addition, the interatomic distances and coordination numbers are directly obtained by the REDD method with the same accuracy for a number of coordination spheres, whereas EXAFS provides these characteristics only for the first coordination sphere. Because of this, the REDD method is successfully used in studies of the phase compositions of nanosystems to identify phases that cannot be determined by conventional phase analysis if the coherent scattering regions are smaller than 3 nm in size. In the REDD method, phase analysis is done using the totality of the interatomic distances and coordination numbers typical of a particular phase (structure) rather than the interplanar spacings and integrated intensities, as is usually done in powder X-ray diffraction analysis (PXD).

There is a number of specific methods which use data on the fine structure of absorption spectra (EXAFS; XANES; near edge X-ray absorption fine structure, or NEXAFS) and are successfully employed to obtain information on the local structure of various materials.[18–25] However, an analysis of such publications goes beyond the scope of this review. We deliberately restricted ourselves to consideration of specific features of the REDD method in order to show, on the one hand, the prospects of its application in studies of any materials (based on inorganic, organic, organometallic compounds) and, on the other hand, to disclose possible difficulties in the interpretation of data on the phase analysis and local structure. Unfortunately, there are almost no publications concerned with structural studies of the same objects using both X-ray diffraction (PDF, REDD) and spectroscopic (XAFS) methods, although they provide complementary information.[25]

A method developed at the G K Boreskov Institute of Catalysis, Siberian Branch of the Russian Academy of Sciences,[26,27] is based on comparison of the model REDD curves calculated for some known well-defined crystal structures with the experimental REDD curves of nanoscale objects of the same chemical composition. It allows one to determine not only the phase composition, but also peculiar features of the local structure of nanomaterials.

II. X-Ray diffraction method of investigation of the radial distribution of electrons: general

1. Relations for calculation of the radial distribution of electrons

The calculated interatomic distances and coordination numbers provide a one-dimensional description of short-range atomic order in a structure; this is similar to the description using the one-dimensional Patterson function. This approach was developed in the mid-20th century and, initially, was mainly used in studies of the local order in liquids (because of the lack of more informative structural methods). The REDD method is based on the integral analysis of the total X-ray scattering intensity curve. Like many other X-ray methods based on the one-dimensional radial distributions, the REDD analysis has intensively developed since 1980s owing to the use of X-ray synchrotron radiation.[19]

Basic to the REDD method is the interrelation between the function of radial distribution of the atomic (electron) density $\rho(r)$ and the intensity of coherent X-ray scattering in the case of diffraction.[28,29] For monatomic systems, one deals with a known equation in spherical coordinates

$$4\pi r^2\rho(r) = 4\pi r^2\rho_0 + \frac{2r}{\pi}\int_0^\infty s\,i(s)\sin(sr)\mathrm{d}s, \quad (1)$$

where r is the interatomic distance,

$$\rho_0 = \frac{dN_A}{M}$$

is the average atomic density per unit volume, d is the picnometric density, N_A is the Avogadro constant and M is the molecular mass,

$$s = \frac{4\pi\sin\theta}{\lambda}$$

is the magnitude of the reciprocal space vector, θ is the Wulf–Bragg angle; λ is the radiation wavelength; $i(s)$ is the coherent scattering intensity obtained from the experimental diffraction intensity corrected for various factors,

$$i(s) = \frac{J(s)}{Nf^2(s) - 1},$$

where $J(s)$ is the measured scattering intensity, N is the number of atoms participating in the scattering and $f(s)$ is the atomic scattering factor.

Since the scattering intensity curve cannot be experimentally measured at infinite limits, calculations using the integral equation (1) are performed using finite integration limits (from S_{min} to S_{max}) corresponding to the measurement range of X-ray scattering. The 'cutoff' effect appearing in this case manifests itself in the appearance of false maxima in the REDD curves (for the identification and taking account of the false maxima, see below).

If a system contains different-type atoms, one uses an approximate solution because for each type of atoms the atomic scattering factor f depends on s in different manner. Usually, the atomic unit factor f_e is introduced as follows:

$$f_e = \frac{\sum_a n_a f_a(s)}{\sum_a n_a k_a},$$

where n_a is the number of the type-'a' atoms in the effective molecule of the object under investigation and k_a is the effective scattering power of the type-'a' atom compared to the unit scattering factor, or the effective number of electrons in the type-'a' atom. The k_a value is determined according to Vainshtein;[30] all atomic scattering factors are normalized to the atomic scattering factor of the lightest atom whose scattering power is set equal to unity.

The relation for calculations of the radial distribution curve for a system comprising different-type atoms remains the same as expression (1), but now it characterizes the radial electron density distribution, and the parameters $\rho(r)$, ρ_0 and $i(s)$ are given by:

$$\rho(r) = \sum_a\sum_b n_a k_a k_b \rho_{ab},$$

$$\rho_0 = \frac{\sum_a (n_a k_a)^2 dN_a}{M},$$

$$i(s) = \frac{J(s)/N - \sum_a n_a f_a^2(s)}{f_e^2(s)},$$

where ρ_{ab} is the electron density distribution over a sphere of the radius r. Equation (1) can be graphically represented by a curve plotted in the coordinates $4\pi r^2\rho(r)$ (Fig. 1). Positions of maxima on this curve correspond to the interatomic distances in the structure. They show at which distances from a given type-'a' atom other atoms are located (equilibrium interatomic distances r), while the areas under the coordination peaks correspond to the number of such atoms located at a given distance (coordination number). It should be noted that each peak in the REDD curve includes all distances from any pair of atoms, thus producing the name of the method, *viz*, analysis of the pair distribution functions of atoms.†

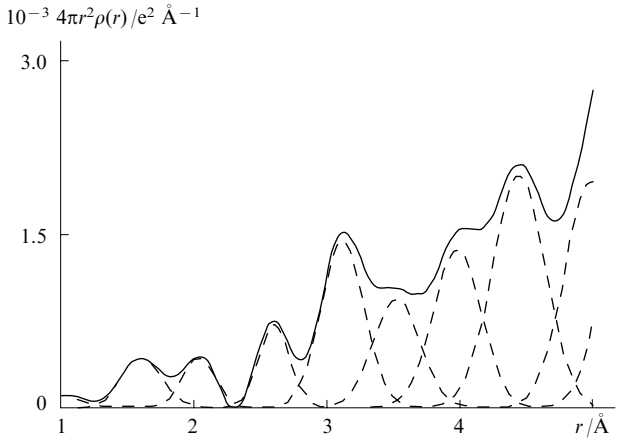


Figure 1. The REDD curve of aluminosilicate.

A significant feature of constructing the REDD curves is that their calculations do not require any assumptions of the structure of the substance under study. The experimental data needed for calculations are as follows: the radiation wavelength, the X-ray scattering intensities collected in a wide range of Bragg angles, the chemical composition of the sample (because calculations are carried out for the effective molecule) and the picnometric density. In addition, possible reference data include the atomic scattering factors, the Compton scattering factors and the absorption coefficients for the elements whose atoms constitute the effective molecule.

2. Experimental designs and data processing

a. Experimental designs

As mentioned above, determination of the distribution of atoms or electrons requires knowledge of the X-ray scattering intensities collected in a wide range of angles with high

† Researchers from France use the abbreviation 'DRD' (Distribution Radiale de la Densite d'electrons) in connection with normalization to electrons and representation of the radial electron density distribution by a spherically symmetric function.[31] More often, only the structural component is represented [as the second addend in the right part of Eqn (1)]; it is refined by the least squares method.[12]

accuracy. The wide range of angles, *viz*., $2^\circ < 2\theta < 155^\circ$, is needed for correct normalization of the scattering intensity curves and correct Fourier transform within wide limits.

X-Ray diffraction studies on laboratory diffractometers are carried out using monochromatized short-wavelength radiation. The monochromator and the sample can be arranged in different manner to provide:

— monochromatization of incident radiation (monochromator is in front of the sample);

— monochromatization of reflected radiation (monochromator is in front of the detector); and

— double monochromatization of the incident and reflected beams.

In the last-mentioned case, it is appropriate to place a bent focusing monochromator in front of the detector in order to reduce the loss of intensity. A particular monochromatization scheme is chosen taking into account the nature of the objects under study (often, it is desirable to eliminate fluorescence from the sample). Double monochromatization is often the only way to correctly exclude the effect of fluorescence under the laboratory conditions.

Effective structural investigations of nanomaterials require high-quality sources of X-ray radiation which should generate high-intensity radiation for high-precision data acquisition over reasonable periods of time and provide the possibility of studying highly dilute systems. Radiation should have a continuous smooth spectrum in a wide range of photon energies to provide the possibility of choosing an appropriate radiation wavelength in particular experiments. This is important for anomalous scattering experiments which are often used in structural studies of samples containing atoms of elements with close atomic numbers [19, 32, 33] or in the case of fluorescent samples.[34–36] In addition, one should know the polarization characteristics of the source to introduce the polarization corrections. All these requirements are met by synchrotron radiation, *i.e*., radiation emitted by an ultrarelativistic charged particle moving along a curved trajectory.[37]

The use of a high-power source of synchrotron radiation not only reduces the exposure time, but also improves the accuracy of experiments and significantly enhances the potential of the REDD method.‡ This first of all concerns the choice of the radiation wavelength. For instance, the use of shorter-wavelength radiation compared to that generated by conventional X-ray tubes allows one to collect a larger experimental data array, which is important for subsequent Fourier transform in connection with the appearance of false peaks due to the cutoff effect. The possibility of choosing λ makes the REDD method selective. Using the effect of anomalous scattering of near-edge atomic absorption of a chosen element, one can calculate the partial radial distribution functions.[19, 32, 33] The advantages of using synchrotron radiation in X-ray diffraction studies of materials are best described in Refs 19 and 37.

‡ Most X-ray diffraction patterns reported in the publications of Russian researchers cited in this review were obtained at the 'Precision Diffractometry and Anomalous Scattering' station, Siberian Centre of Synchrotron and Terahertz Radiation (Budker Institute of Nuclear Physics, Siberian Branch of the Russian Academy of Sciences) using a diffraction beam with Si (111) monochromator crystal (degree of monochromatization $\Delta\lambda/\lambda \approx 10^{-4}$).

b. Normalization

Correct calculations of the REDD curves require that the scattering intensity curves be corrected for the background, polarization, absorption and that the small-angle and Compton (incoherent) X-ray scattering be excluded (either computationally or experimentally). Particular difficulties are associated with exact determination of the intensity at large angles, the inclusion of Compton scattering and exact specification of the atomic scattering curves, because these curves are sometimes chosen with unknown bond ionicities or the effective atomic charges. To eliminate these difficulties, an original technique was used,[34–36, 38–40] namely, the atomic scattering factors were calculated from the measured intensity curve processed in a specific manner (the experimental curve was smoothed using the fitting polynomials). Since measurements of the $J(s)$ curve in the sub-zero region are problematic, tabulated data for the atomic scattering factors are used as a rule for small s (from 0 to 1 Å^{-1}).

The scattering factors f are expressed in electronic units; therefore, the experimental intensity curves should be converted to these units, *i.e*., normalized. In essence, a correct normalization underlies the reliability of the REDD curves; therefore, researchers pay particular attention to this procedure. Factors affecting normalization of the intensity curves in the REDD method were analyzed.[38] We believe that it is appropriate to perform a double normalization including a conventional normalization to 'tails' of the intensity curve (at large Bragg angles) followed by the normalization according to Vainshtein [30] (to the area under the normalized scattering curve). Normalization to 'tails' is based on the fact that at large scattering angles the interference effects are weak and the experimental curves (scattering intensity is measured in counts) differ from the theoretical ones (scattering intensity is expressed in electronic units) by a constant. However, such a normalization is not always correct because the measurement errors at large angles are larger than the errors in the mid-range of the curve and amount to 10%–20%. Subsequent normalization to the area under the whole experimental curve is based on the energy conservation law, according to which the integral of the intensity of coherent scattering from N molecules over the reciprocal space equals the integral of independent atomic scattering

$$\int_0^\infty \frac{J(s)}{N} s^2 \mathrm{d}s = C_S \sum_{a=1}^{m} n_\mathrm{a} f_\mathrm{a}^2(s) s^2 \mathrm{d}s.$$

In the case of double normalization, provided a correctly performed experiment with inclusion of all corrections, the normalization factor C_S should be close to unity. Otherwise, false peaks appear on the experimental REDD curves, which do not correspond to the structure of the material under study. False peaks on the REDD curves is the main reason why the REDD method is of limited use. Processing of experimental scattering intensity curves for calculations of the REDD curves have been well documented.[8, 38] Figure 2*a* presents the unnormalized, raw, as well the normalized and smoothed scattering intensity curves at large angles while Fig. 2*b* shows the corresponding REDD curves for γ-Al_2O_3 support. As can be seen, main peaks on the REDD curves plotted using the raw, unnormalized intensity curves are shifted and false peaks appear.

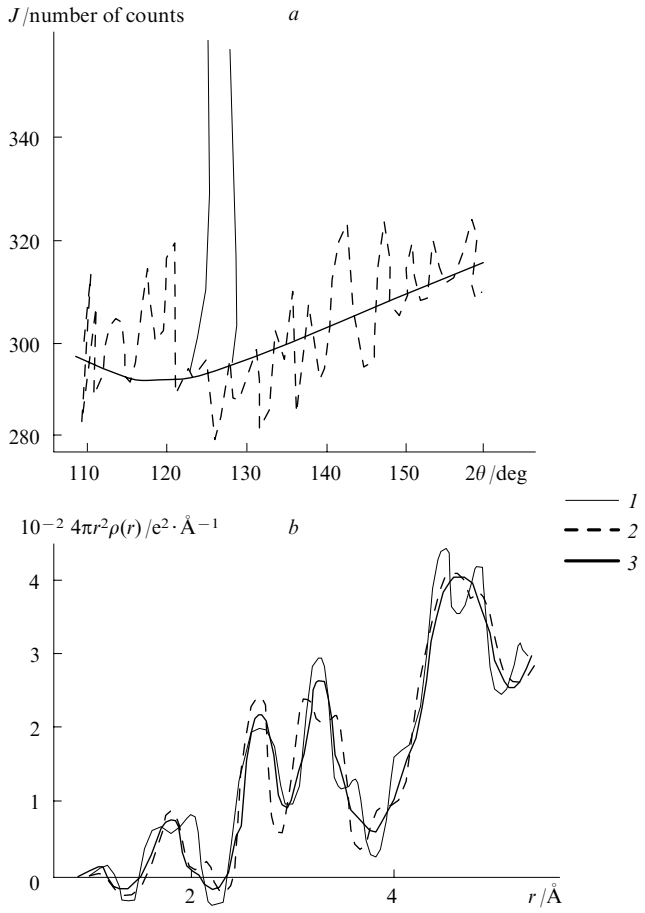


Figure 2. Experimental scattering intensity curves (*a*) at large angles: raw data (*1*), unnormalized data (*2*), normalized and smoothed data (*3*) and the corresponding REDD curves (*b*).[38]

3. Constructing the difference curves of the radial electron density distribution

The problem of correctness of the REDD curves is particularly topical when comparing a number of curves[38,39] in, *e.g.*, studies of samples of identical chemical composition obtained under different conditions or post-synthesis treated in different manner. In addition, the problem of structural additivity arises in the formation of a multicomponent system because the structure of the system can be distorted due to changes in the phase composition caused by the interaction between the phases as one of them is coated onto the other (in, *e.g.*, coating of the active component onto the support during the synthesis of supported catalysts, film deposition onto the support, *etc.*). Assuming that the active component does not interact with the support, one can construct the difference curves of the radial electron density distribution which describe the structure of the active component only. The difference curves provide additional information on the structure of the catalytic system.[8,38–45] Construction of the difference curves of the radial electron density distribution begins with constructing the REDD curves of the catalyst and support followed by recalculation using corrections for different average densities. Then, the difference curves of the radial electron density distribution are constructed.

Investigations of materials containing interaction phases are much more complicated. In the case of supported catalysts, an analysis of the difference curves of the radial electron density distribution suggests the state of the active component and the expected changes in the support upon the interaction with the active component. Also, preliminary construction of the difference intensity curve is believed to be useful.[38–41] However, construction based on the initial (unnormalized) intensity curves, even obtained under identical experimental conditions, is incorrect due to different depth of the 'operating' layer which reflects X-rays from the support and the catalyst whose active component usually contains heavy atoms. The subtraction procedure should be performed using the curves for which the scattering intensity is converted to electronic units. Prior to subtraction, the equations of the scattering intensity curves of the catalyst and support are augmented with the corrections mentioned above and then normalization is carried out. The difference intensity curve is constructed assuming that the diffraction maxima of the catalyst and support are described by the same analytical functions, which undoubtedly is only a first approximation. When the substructural characteristics of the support phase in the catalyst change (particle size changes or microdistortions appear), which leads to changes in the widths and profiles of the diffraction peaks of this phase, minima may appear on the difference intensity curve. Then, this curve is used to construct the difference curves of the radial electron density distribution.

Figure 3 illustrates construction of the difference curve of the radial electron density distribution for a catalyst

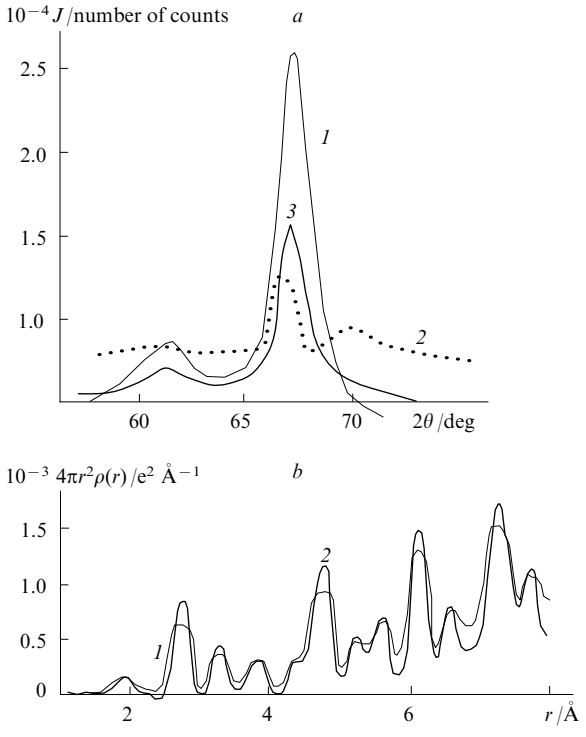


Figure 3. Portions of unnormalized curves for the support η-Al_2O_3 (*1*), the difference intensity curve (*2*), catalyst 10% Ir on η-Al_2O_3 (*3*) (*a*) and the corresponding difference curves of the REDD constructed using the difference intensity curve (*1*) and the REDD curves (*2*) (*b*).[39]

containing 10% Ir supported on η-Al_2O_3. The difference intensity curve exhibits a diffraction peak characterizing the metallic iridium phase ($2\theta = 69.2^\circ$) and a peak of a phase whose unit cell parameter is larger than that of the support (the diffraction peak of this phase is shifted towards smaller angles). It was shown that the latter peak characterizes the interaction phase which is formed during the synthesis of the catalyst. An *interface* phase is formed on the support surface, namely, iridium ions initially present in the precursor (hexachloroiridic acid) whose solution is used to impregnate the support, are implanted into the support. A similar phase was also discovered in an Al/Pt catalyst.[8] It was shown that the interaction phase possesses specific catalytic properties. For instance, studies[42,43] of a supported Al/Pt catalyst showed that metallic platinum particles are active in the dehydrogenation of cyclohexane while the phase containing Pt ions is active in the dehydrocyclization of n-heptane.

The contributions of certain pairs of atoms to the REDD curves can also be determined using the anomalous scattering effect.[19,25,33] By measuring the scattering intensity near and far from the absorption edge of a particular atom one can construct a difference intensity curve and then the partial REDD curve. For instance, the phase composition of a European standard Pt/SiO_2 catalyst and the possibility of formation of the interaction phase between the active component and support were determined[33] in a diffraction experiment using the effect of anomalous scattering and synchrotron radiation.

4. Parameters determined from the radial electron density distribution curves

As mentioned above, the interatomic distances r in the structure are determined from positions of coordination peaks in the REDD curves. The coordination number (Z) is calculated from the areas under the coordination maxima (S) using the relation

$$S = n_a k_a^2 Z_{aa}$$

for identical atoms and

$$S = n_a k_a k_b Z_{ab},$$

for different atoms. Here n_a is the number of the type-'a' atoms and k_a and k_b are the scattering powers of the type-'a' and type-'b' atoms, respectively.

In addition, the REDD curves allow one to evaluate the size of the coherent scattering region (distance at which atomic positions are no longer correlated) for small particles.[27,34–36,44,45] The REDD curves of small particles exhibit no coordination peaks and $\rho(r) = \rho_0$. A corresponding example is shown in Fig. 4.

The accuracy of determination of structural parameters from the REDD curve is affected by the following factors:

— approximate character of the equations related the structural characteristics to the angular distribution of the scattering intensity;

— insufficient accuracy of determination of the f-factors for coherent and Compton scattering; and

— correctness of the normalization procedure.

Usually, the scattering intensity curve is constructed with a deviation of 2%–3%. The highest accuracy of determination of structural parameters is attained using the double normalization procedure and experimental atomic scattering factors. In this case, positions of and areas under coordination peaks are determined with relative errors of $\pm 0.5\%$ and $\pm 5\%$, respectively.

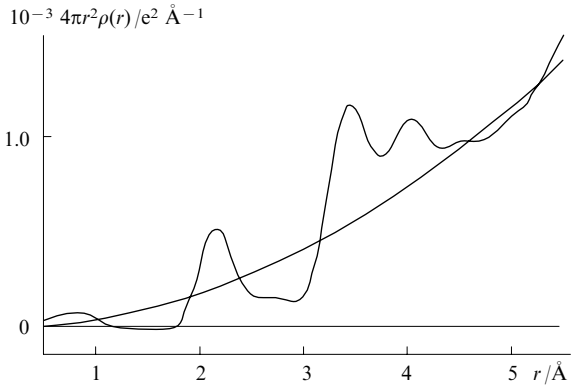


Figure 4. The REDD curve for zirconia with the coherent scattering region smaller than 15 Å.[36]

The REDD curves are characterized by diffuse overlapping peaks. The main reasons for diffuse character of the peaks include thermal atomic vibrations near the equilibrium positions and statistical scatter of the equilibrium positions. Determination of the root-mean-square atomic displacements[29,46] from the peak widths in the RDA curves is incorrect.

Various methods for calculation of areas under overlapped peaks are available, *viz*., construction of the right wing using the left one (symmetric mapping), integration to the first minimum, *etc*. Maxima (see Fig. 1) were also separated[9,26,27] by modelling with the modified Gaussian function and representing the whole REDD curve by the sum of Gaussians

$$4\pi r^2\rho(r) = \sum_i A_i \frac{r^2}{r_i^2} \exp\left[-\frac{(r-r_i)^2}{2b_i^2}\right], \qquad (2)$$

where r_i is the equilibrium position of the ith maximum, A_i is its amplitude and b_i is the root-mean-square deviation. It should be noted that the true coordination number and the coordination number determined from the area under the coordination peak are different,[46] the latter being dependent on the maximum magnitude of the reciprocal space vector (s_{max}).

III. Comparative method of the radial electron density distribution

1. Constructing model curves of the radial electron density distribution

Owing to specific features of nanomaterials and ambiguity of structural information obtained experimentally, structural data on these systems sometimes differ from the structural data for known phases. In this connection, one should compare the experimental REDD curves with the model curves constructed for possible constituent phases with the known structures.[26] The method of construction of the model curves allows one not only to identify the phase composition of nanocomposites, but also to reveal structural features of constituent phases.

The areas under the coordination peaks on the REDD curve depend on the coordination numbers; this was used to construct the model curves [9, 26, 47, 48] for known structures. If exact chemical composition of a sample is known, one can assess the phase composition. Using known structural data (unit cell parameters, space groups, atomic coordinates and occupation numbers of atomic positions in the unit cell), the interatomic distances and coordination numbers are calculated for each structure. Usually, structural data from various databases [49] and handbooks (see, *e.g.*, Ref. 50) are used. The interatomic distances and coordination numbers can be calculated using, *e.g.*, the ICSD/Retrieve and POLYCRYSTAL [51] databases. Next, having determined the necessary values of the effective number of electrons (k_a) from the relations given above, one can calculate the areas under coordination peaks.

When the model curves are represented by the sum of Gaussian functions, the pre-exponent in Eqn (2) is written for convenience in another manner. The relation has the form

$$4\pi r^2 \rho_{\text{mod}}(r) = \sum_i \frac{S_i}{(2\pi)^{1/2} b_i (1 + b_i^2/r_i^2)} \frac{r^2}{r_i^2} \exp\left[-\frac{(r - r_i)^2}{2b_i^2}\right], \quad (3)$$

where S_i is the area under the ith coordination maximum. The model curves [26, 27] were constructed using an α-Al_2O_3 standard sample provided by the International Centre for Diffraction Data.

From relation (3) for calculation of the model REDD curves it follows that one can also calculate the 'partial' components of the REDD curve, corresponding to the distribution of distances between different types of atoms.

After construction of the partial model curves, they are compared with particular portions of the experimental curves. It is this procedure that is employed to determine changes in the experimental curves, characteristic of particular structural fragments, *e.g.*, the cation and anion sublattices in ionic compounds, individual layers in layered structures, *etc*.

The results of calculations of the total and partial model curves of a layered structure of crystallized aluminium hydroxide AlOOH (boehmite phase) are shown in Fig. 5. Constructing such model curves enabled structure characterization of pseudoboehmites (nanomaterials) obtained in various experiments and allowed one to relate their structural parameters to other physicochemical properties.[48, 52, 53]

One can also construct the model REDD curves for mixed phases and use them in the phase analysis of nanocomposites. The total model curve is described by the expression

$$4\pi r^2 \rho_{\text{mod}}(r) = 4\pi r^2 \sum_a c_a \rho_a(r),$$

where $4\pi r^2 \rho_a(r)$ is the model REDD function of a particular constituent phase and c_a is the content of this phase.

When considering the catalytic properties of modified catalysts, it is important to know whether the dopant forms an individual phase in the support or catalyst, or it is a constituent of the main component. Often, doping leads to formation of solid solutions. The model REDD curves for

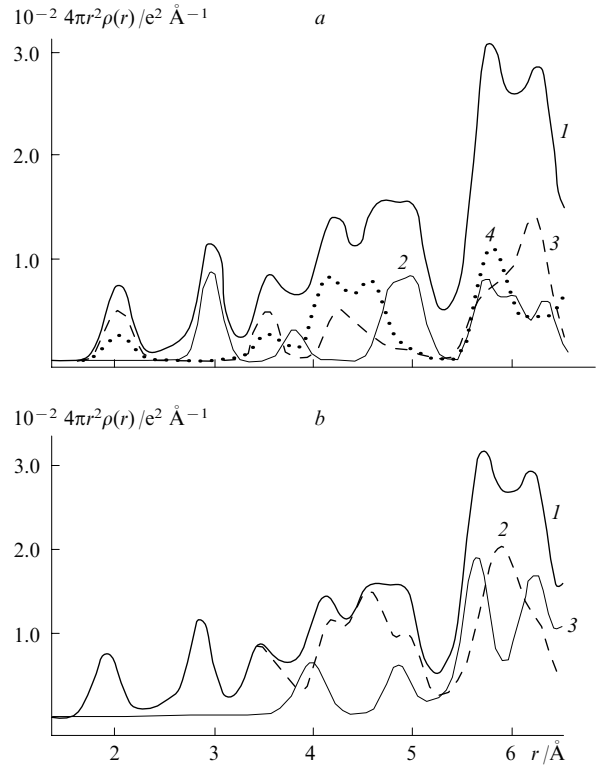


Figure 5. Model REDD curves.
(*a*) For the structure of crystallized boehmite (*1*) and the partial curves for the distances Al−Al (*2*), Al−OH (*3*) and Al−O (*4*); (*b*) for the structure of crystallized boehmite (*1*) and the partial curves for the contributions of the intra-layer (*2*) and inter-layer (*3*) distances.

substitution solid solutions were constructed.[54–56] Usually, the structural type (space group and atomic coordinates) of such systems remains unchanged, while the unit cell parameters and the scattering power of atoms vary. In this case, the interatomic distances change in proportion to the ratio of the unit cell parameters of the solid solution to the initial structure and there is no need to recalculate all interatomic distances; it is sufficient to augment expression (3) with the corresponding normalization factor. Since the atoms to be replaced and the dopant atoms occupy the lattice sites randomly, the areas under corresponding coordination peaks are calculated using the averaged effective number of electrons

$$K_{\text{cp}} = \frac{\sum n_i K_i}{\sum n_i},$$

where K_i is the effective number of electrons in the atoms occupying identical crystallographic positions and n_i is the number of such atoms in the formula unit of the compounds under study.

By comparing the experimental REDD curve of a solid solution and the corresponding model curve one cannot only detect short-range changes in the structure but also identify highly disperse or X-ray amorphous phases which are not detected by conventional powder X-ray diffraction.

2. Identification and taking account of false peaks due to the cutoff effect

As mentioned above, the cutoff effect due to a decrease in the integration limits manifests itself when doing the Fourier transform of the experimental scattering intensity curve and solving Eqn (1). As a result, false peaks appear on the REDD curve near each true electron density maximum; they may overlap with the nearest maxima. This effect is particularly pronounced in the studies of structures characterized by strongly different *f*-factors, when intense false peaks from 'strong' maxima corresponding to the distances between heavy atoms are superimposed on the 'weak' maxima characterizing the distances between light atoms. False peaks arrange symmetrically on both sides of the main maximum. Their positions are determined from the relation

$$r = r_0 \pm \frac{2.5\pi}{s_{\max}},$$

where r_0 is the position of the true maximum. By varying $s_{\max}$ one can reveal false peaks (their positions vary); however, their intensities and, as a consequence, contributions in the case of overlap with true maxima are difficult to determine.

To reduce the effect of false peaks when calculating the experimental REDD curves, an artificial temperature factor is usually introduced [29, 46]

$$f_T = \exp(-bs^2),$$

(b is the damping factor) and multiplied by the intensity function $i(s)$. Figure 6 illustrates the changes in the REDD curve upon introducing the damping factor. All peaks become diffuse, their resolution becomes poorer, but the problem of distinguishing between the false and true maxima still persists.

In this case, a comparison of the experimental and model REDD curves may lead to incorrect interpretation of the changes in the local structure. However, this drawback of the comparative method can be eliminated. At the same time, the model REDD curves were calculated [26, 57] with no Fourier transform and the curves showed no false peaks.

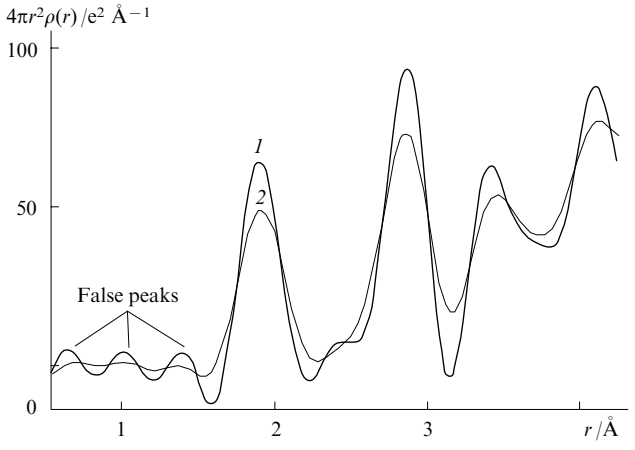


Figure 6. Experimental REDD curve for boehmite calculated without (*1*) and with a damping factor (*2*).

It is appropriate (we believe, correctly) to compare the model and experimental REDD curves which show identical cutoff peaks. In other words, the false peaks should not be excluded from the experimental REDD curve; rather, the model curves should be calculated with inclusion of the false peaks. A comprehensive analysis of the cutoff effect on the REDD curve was reported.[58] Taking into account the available recommendations,[58] the procedure for calculating the model curves was modified [57] by introducing the convolution of the function of the interatomic distances

$$G(r) = \frac{2}{\pi}\int_0^\infty s\, i(s)\, \sin(sr)\mathrm{d}s$$

with the cutoff function

$$g(r) = \frac{\sin(r\, s_{\max})}{\pi r}.$$

The modified model curves were calculated using the relation

$$4\pi r^2\rho_{\mathrm{mod}}(r) = G^*(r)\, r + 4\pi r^2\rho_0,$$

where $G^*(r)$ is the modified function of interatomic distances. The procedure [57] for calculations of the model curves with inclusion of the cutoff effect was tested on a reference sample of α-Al_2O_3 (Fig. 7). A comparison of the experimental REDD curve with the model curve having no false peaks revealed poor agreement (see Fig. 7 *a*), whereas the model curve constructed taking into account the cutoff effect almost matches the experimental REDD curve (see Fig. 7 *b*). It is important that in the latter case, the exper-

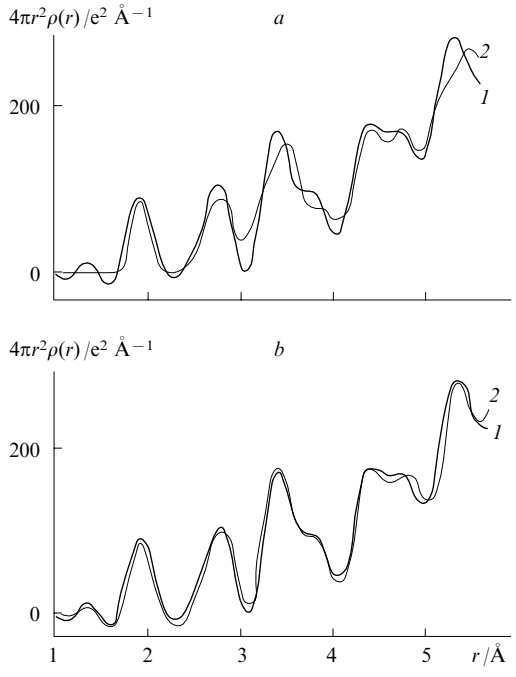


Figure 7. A comparison of the experimental REDD curve for α-Al_2O_3 (*1*) with the model curve (*2*) calculated ignoring (*a*) and including the cutoff effect (*b*).[57]

imental REDD curve is not damped and its profile remains undistorted.

Construction of the model curves in the comparative method extends the field of its application, *viz*., one can also investigate crystallized materials. Usually, such objects are difficult to study by the REDD method because their diffraction patterns show large numbers of wide-angle peaks. This leads to poor normalization and the appearance of false peaks on the REDD curves. Calculations of the model curves with inclusion of the false peaks eliminates errors in the identification of structural peaks. Figure 8 illustrates excellent agreement between the experimental and model (with inclusion of false peaks) REDD curves for well-crystallized ceria. Almost perfect coincidence (*R*-factor is 1.3%) of the model and experimental REDD curves suggests that the local structure of coarse-grained ceria does not differ from the perfect fluorite structure and that the procedure for introduction of false peaks into the model REDD curve (see above) is correct.

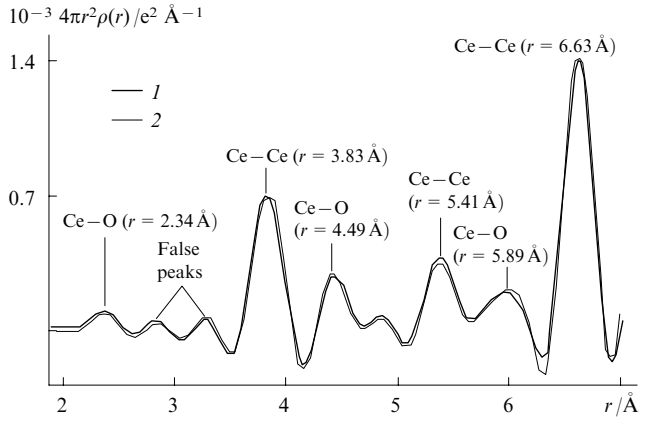


Figure 8. The experimental (*1*) and model (*2*) REDD curves for CeO_2.[27] Curve (*2*) shows false peaks.

IV. Investigations of oxide supports for catalysts

The properties of catalysts depend on the structural features of the active component and support and on their mutual influence.[59] These aspects are of particular importance for structure diagnostics of catalysts.

1. Aluminium oxides

Aluminium oxides exhibit unique properties and are used as components and supports in the synthesis of many metallic and oxide catalysts including catalysts for oil and gas processing. In addition, these high-tech materials are widely used in the preparation of ceramics, as adsorbents for dehydration of liquids and gases, *etc*. The properties of aluminium oxides are determined by the structural features of numerous polymorphs whose stabilization in turn depends on the starting hydroxide and on the temperature regime of its dehydration.[60] Dehydration of hydroxides is accompanied by the formation of polymorphs as temperature increases. Aluminum oxides have the general formula $Al_2O_3 \cdot n\,H_2O$, where $0 \leqslant n < 0.6$.[61, 62] A complete dehydration results in the stable phase α-Al_2O_3, the only oxide containing no OH groups. Other polymorphs, in particular, low-temperature (γ, η, χ) and high-temperature (δ- and θ-Al_2O_3) ones, are metastable and occupy an intermediate position in the system aluminium hydroxide – aluminium oxide. Metastable low-temperature aluminium oxides crystallize in a spinel-like structural type and have the general structural formula $A^*_{x1}A_{x2}B^*_{y1}B_{y2}O_{32-z}(OH)_z$, where A and A* are the positions of aluminium cations in the tetrahedral environment, B and B* are the positions of cations in the octahedral environment in the spinel structure and A* and B* are the non-spinel positions§ in the space group *Fd*3*m* (Ref. 63). Differences between metastable polymorphs are mainly due to the existence of defects or to the nature of surface-forming planes.[64] This leads to different types of joining of nanoblocks with the spinel structure and to formation of different types of nanostructures.[65] Table 1 lists the structural formulas of the low-temperature forms of aluminium oxide obtained using the results of FPA of diffraction patterns.

Table 1. Structural formulas according to FPA of diffraction patterns for γ- and η-Al_2O_3.

Polymorph	Starting hydroxide	Formula
γ-Al_2O_3	Boehmite	$A^*_{1.75}A_{5.5}B^*_{2.0}B_{9.0}O_{22.75}OH)_{9.25}$ $(Al_2O_3 \cdot 0.5\,H_2O)$
γ-Al_2O_3	Pseudoboehmite	$A^*_{1.75}A_{6.75}B^*_{1.0}B_{9.0}O_{23.5}(OH)_{8.5}$ $(Al_2O_3 \cdot 0.46\,H_2O)$
η-Al_2O_3	Bayerite	$A^*_{1.5}A_{6.75}B^*_{1.0}B_{10.0}O_{25.75}(OH)_{6.25}$ $(Al_2O_3 \cdot 0.32\,H_2O)$

To conserve the valence balance, aluminium oxides are usually represented[60] as defect spinels with vacancies having the general formula $Al_{21.33}\square_{2.67}O_{32}$ (where $\square$ stands for a vacancy). The model REDD curves for aluminium oxides were calculated[66] assuming the defect spinel structure with vacancies. The following limiting cases with respect to occupation of cation positions were considered:

model 1 — all cation positions in tetrahedral environment are occupied and all vacancies are at the centres of octahedra (structural formula $A_8B_{13.33}\square_{2.67}O_{32}$);

model 2 — all positions at the centres of octahedra are occupied and vacancies are at the centres of tetrahedra (structural formula $A_{5.33}\square_{2.67}B_{16}O_{32}$).

The total and partial REDD curves constructed for these models with inclusion of the contributions of different types of distances, *viz*., A–A, B–B, A–B, A–O and B–O are presented in Fig. 9. The partial REDD curves show which portions of the total curve correspond to occupation of particular positions. As can be seen, vacancies at the centres of tetrahedra (model 2) are responsible for the decrease in the REDD curve in the region $r \approx 3.3$ Å because the number of the distances A–A and A–O decreases. In addition, the electron density in the region $r \approx 4.5$ Å increases due to a large number of occupied octahedra in this model structure. These data can be used

§ In the spinel structural type, eight tetrahedral and sixteen octahedral voids in the close packing of oxygen ions are filled. Other voids are unfilled; otherwise, one deals with a deviation from the spinel structural type.

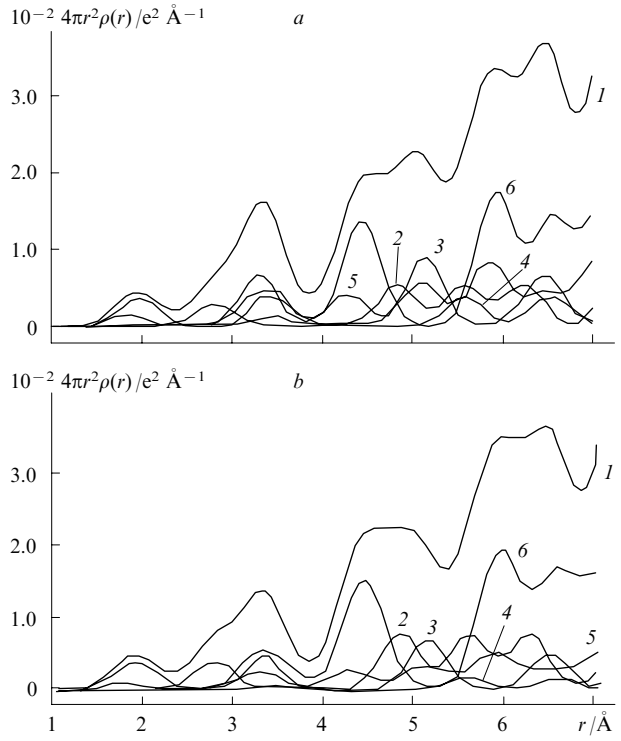


Figure 9. Partial REDD curves showing the contributions of particular distances to the total REDD curve; plotted for different structure models of aluminium oxide.[26]
(*a*) For model 1 (vacancies only in octahedral cation positions), (*b*) for model 2 (vacancies only in tetrahedral positions). (*1*) Total curve, (*2*) B–B, (*3*) A–B, (*4*) A–A, (*5*) A–O, (*6*) B–O.

in the analysis of the structure of low-temperature aluminium oxides obtained in different experiments.[53]

2. Cerium dioxides

Owing to low redox potential of the Ce^{4+}/Ce^{3+} pair (1.61 eV) ceria can readily add and donate oxygen (due to the transition $Ce^{3+} \rightleftarrows Ce^{4+}$) depending on the partial pressure of oxygen in the gas phase. The operating efficiency of this material in redox processes can be assessed in terms of the oxygen capacity. At low oxygen pressure, raising the temperature causes ceria to undergo reduction with the formation of a continuous series of oxygen-deficient nonstoichiometric oxides CeO_{2-x} with the fluorite-like structure characterized by disordering of oxygen vacancies. On lowering the temperature these oxides form highly organized fluorite-like superstructures of the general formula Ce_nO_{2n-m}. The structures of a few oxides are known, namely, Ce_7O_{12}, $Ce_{11}O_{20}$,[67] Ce_6O_{11}.[68] They contain ordered anion vacancies. The known oxides with ordered vacancies and pyrochlore-like structures have the general formula A_4O_7 (A is cation). Non-stoichiometric cerium oxides are rapidly oxidized in air.

The formation of non-stoichiometric cerium oxides CeO_{2-x} may shift the valence balance either due to changes in the anion sublattice and the appearance of oxygen vacancies or due to filling of interstices by cations and occupation of cation vacancies by excess oxygen atoms. The excess charge that appears in the CeO_{2-x} oxides as a result of cerium reduction is compensated by the formation of vacancies in the oxygen sublattice.[69, 70]

Ceria exhibits increased susceptibility to reduction when present in a highly disperse state. At 10-nm CeO_2 crystallite size, the heat of reduction is halved.[71] Oxygen vacancies on the surface of ceria particles are more stable than in the bulk.[72, 73] In turn, the diffusion mobility of oxygen ions depends strongly on the degree of dispersion and on the defectiveness of the oxide structures. Therefore, despite the fact that the stable phases of cerium dioxides have been studied in detail, investigations of defects in the averaged and local structures (on the size scale of 1–3 unit cells) of highly disperse cerium dioxides and the effect of dopant cations are still topical. It is these cerium dioxides that are used as supports for catalysts for CO oxidation in hydrogen-containing gas mixtures.[74–80]

The structural and substructural characteristics, the local structures of CeO_2 samples synthesized under different conditions and having different degree of dispersion were compared to study the effect of the particle size on the structure of CeO_2.[27, 81, 82] The oxides with the 120- and 140-Å coherent scattering regions (D) were prepared by thermal decomposition of cerium nitrate and cerium ammonium nitrate, respectively, while the oxide with D = 50 Å was synthesized from ester polymeric precursors. A sample of coarse-grained ceria with $D > 1000$ Å was used for comparison. A FPA of diffraction patterns showed that, irrespective of the degree of dispersion, the averaged structure of the CeO_2 samples is quite reliably described by a fluorite-type cubic structure (space group $Fm\bar{3}m$).

However, the REDD study of the local structure of the oxides with different degree of dispersion revealed some features. Naturally, the short-range atomic order in coarse-grained ceria corresponds to a perfect fluorite structure (see Fig. 8). The sample comprised of the smallest particles exhibited the most pronounced changes in the short-range order of ions in both the cation and anion sublattices, namely, a decrease in the coordination numbers corresponding to the Ce–Ce peaks and an increase in the coordination numbers for the Ce–O peaks (Fig. 10). The Ce–Ce peaks on the experimental REDD curves constructed for the samples obtained by thermal decomposition of salts matched the corresponding peaks on the model REDD curves; also, an additional electron density appeared in the region of the peaks corresponding to the Ce–O distances on the experimental REDD curves, which sug-

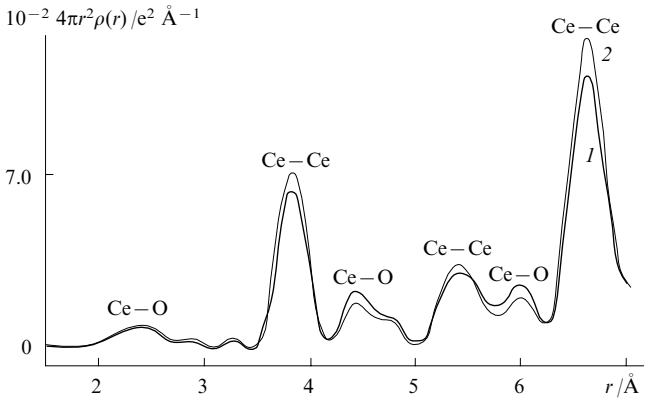


Figure 10. The REDD curve for ceria sample with D = 50 Å (*1*) and the model REDD curve for CeO_2 (*2*).[27]

gested changes in the anion sublattice. Different explanations for these changes were proposed.

a. Filling of interstices by oxygen ions as a defect in the anion sublattice

The possibility for a Frenkel defect to occur in the anion sublattice of CeO_2 has been a subject of discussion; indeed, about 20% of oxygen ions are displaced from the regular positions in the fluorite structure along the [111] direction to the interstices with octahedral cation environment (Fig. 11).[83] The model REDD curves were constructed [27, 82] taking account of this type of defects. A comparison of the experimental REDD curve with the model curves constructed for a perfect structure and for a defect structure of the samples with $D = 120$ and 140 Å, showed that the introduction of the defect provides no explanation for the changes in the Ce—O peak ($r = 2.34$ Å) and for the increase in the area under the Ce—O peak ($r = 4.49$ Å); on the contrary, this peak weakens if a displacement exists (Fig. 12). Thus, it was shown that in the highly disperse oxides studied the oxygen ions are not displaced to the interstices. We believe that this defect may appear at high temperatures when the ion mobility enhances; indeed, this was actually detected.[84]

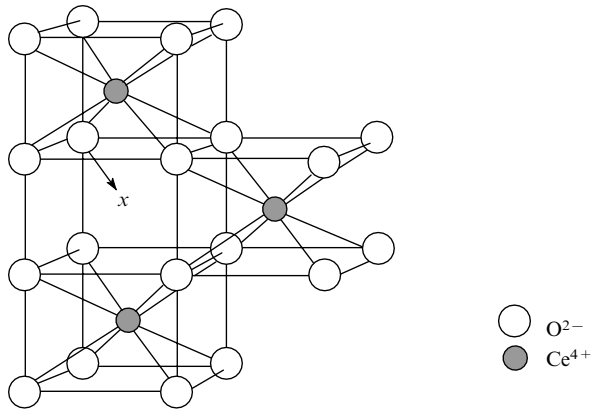


Figure 11. Frenkel defect in the anion sublattice of CeO_2.

An erroneous conclusion about the existence of this type of defects in the structure of a highly disperse oxide [83] may be due to the fact that the REDD curves were analyzed ignoring the possibility for false peaks to exist. The authors of that study used neutron radiation (it is the most sensitive to scattering of oxygen atoms) for the best identification of Ce—O bonds. Indeed, the coordination peaks corresponding to Ce—O distances on the RDA curves are much more intense than in the case of X-ray radiation. However, the corresponding false peaks are also intense and should be taken into account. Additional peaks on the experimental REDD curve [83] may also be due to the impurity (lanthanum oxide, 3%) present in the sample. This conclusion was also reported in a monograph.[85]

b. Compositional defect in the anion sublattice

Additional peaks on the REDD curves may be due to the presence of residual anionic groups from precursor salts (cerium nitrate crystal hydrates) in the oxide structures. To identify this defect, the partial model REDD curves with maxima corresponding to the Ce—NO_3^- and Ce—OH^- distances in cerium nitrate and cerium hydroxide were constructed and compared with the REDD curves for the samples with $D = 120$ and 140 Å.[27] The curves in Fig. 13 show that the additional electron density in the region $r \approx 2.5-2.6$ Å is due to the appearance of distances between cerium cations and new anionic groups. In other words, the structure of the disperse CeO_2 samples synthesized from nitrate salts is characterized by disordering only in the anion sublattice owing to the presence of residual NO_3^- and OH^- groups. The existence of residual groups in the anion sublattice of the oxide was confirmed by IR spectroscopy. It was shown that these defects in the anion sublattice stabilize the disperse state of the oxides. A complete X-ray diffraction study showed that ceria synthesized from cerium ammonium nitrate contains a smaller amount of additional anionic groups, has a larger lattice constant, considerable microdistortions and is characterized by incomplete occupation of positions of oxygen atoms (this indicates vacancies in the structure) compared to the oxide synthesized from cerium nitrate.[79] Taking into account these structural features, the former oxide was chosen to

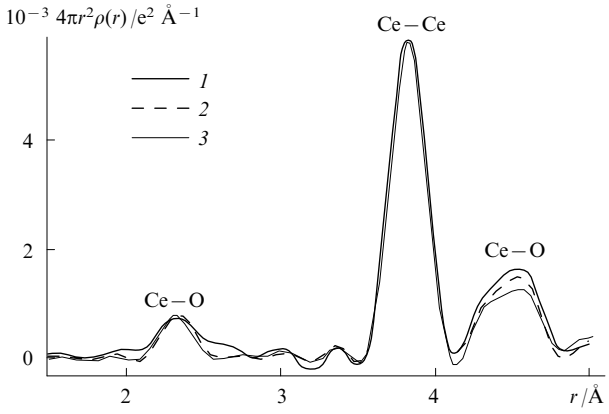


Figure 12. Experimental REDD curve for ceria sample with $D = 120-140$ Å (*1*) and the model curves for perfect CeO_2 structure (*2*) and for the structure containing a Frenkel defect (*3*).[27]

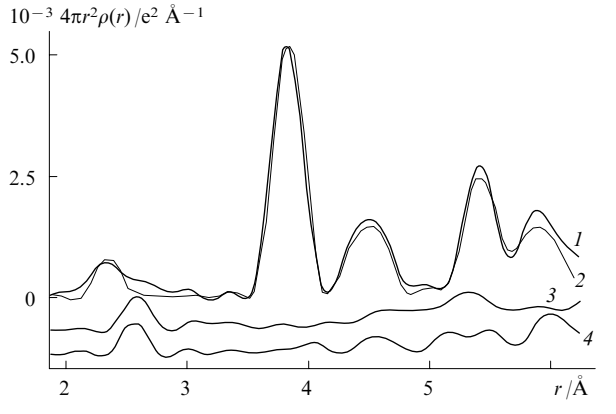


Figure 13. Experimental REDD curve for CeO_2 sample with $D = 120$ Å (*1*), the model curve for CeO_2 (*2*) and the partial REDD curves for cerium nitrate (*3*) and cerium hydroxide (*4*).[27]

be a component acting as a reversible source of oxygen for the copper–cerium catalyst.[86, 87]

c. The structures of modified cerium oxides

The oxygen capacity of pure ceria is low and often insufficient for efficient operation of catalysts. In addition, pure ceria is thermally unstable and its specific surface area considerably decreases as temperature increases. To improve the useful properties of ceria, it is modified by doping with cations replacing cerium ions.[88]

Cerium–samarium oxides. The local structure of mixed cerium–samarium oxides was studied[89] using $Ce_{1-x}Sm_xO_{2-x/2}$ ($x = 0.1$, 0.2, 0.4) samples synthesized from polymeric precursors by a method that allows one to avoid nonuniform distribution of dopant cations over the volume of the sample. Samples were heat treated in air for 4 h at 500 and 700 °C. Powder X-ray diffraction analysis of the samples showed that all of them were single-phase systems of ceria-based solid solutions with the fluorite structural type. Analysis of the unit cell parameters and D values showed that doping with larger samarium ions causes the unit cell parameter of the solid solution to increase and that the D value is to a greater extent determined by the calcination temperature rather than by the composition of the solid solution.

Oxides with a distorted fluorite structure can have vacancies in the anion sublattice and are described by the general formula M_nO_{2n-2} (M is cation).[90, 91] This series begins with the structures MO_2 and M_2O_3 including CeO_2 and Sm_2O_3. The interatomic distances and coordination numbers for these structures were calculated from crystallographic data. The interatomic distances appeared to be close but the patterns of the first coordination sphere are different (Fig. 14). The Ce–Ce distances in CeO_2 are 3.83 Å and the coordination number of the Ce atoms is 12. In the Sm_2O_3 structure, the Sm–Sm distances are 3.62 and 4.12 Å and all atoms have a coordination number of 6. In addition, samarium oxide shows a range of Sm–O distances (from 4.05 to 5.09 Å), whereas CeO_2 is characterized by one Ce–O distance in this region (4.49 Å); the coordination number is 12. To elucidate whether the solid solution contains clusters with the Sm_2O_3 structure, the model REDD curves for CeO_2, Sm_2O_3 and a solid solution $Ce_{0.6}Sm_{0.4}O_{1.8}$ with the fluorite structure and a unit cell parameter of 5.445 Å were constructed. In addition, the REDD curve for a mechanical mixture of phases of pure oxides taken in the corresponding ratio was modelled. Some portions of these curves, as well as the REDD curve for the $Ce_{0.6}Sm_{0.4}O_{1.8}$ sample calcined at 700 °C are shown in Fig. 14. The experimental REDD curve for the mixed oxide under investigation differs from both the model curves for individual oxides and from the REDD curve for their mixture. Table 2 lists the interatomic distances and coordination numbers for the structures of CeO_2, a perfect solid solution $Ce_{0.6}Sm_{0.4}O_{1.8}$ and the experimental data for the $Ce_{0.6}Sm_{0.4}O_{1.8}$ sample. The most pronounced difference of the structure of the sample under study was found at short distances. For instance, the first coordination peaks for the metal–oxygen (Ce–O) and metal–metal (Ce–Ce) distances are split. The Ce–O peaks for the second coordination sphere are also split. Positions of the Ce–Ce peaks for the second and third coordination spheres almost coincide with the distances in the structure of the solid solution (5.48, 6.67 Å). The Ce–O interatomic distances (5.97, 7.07 Å) are 'averaged' analogously.

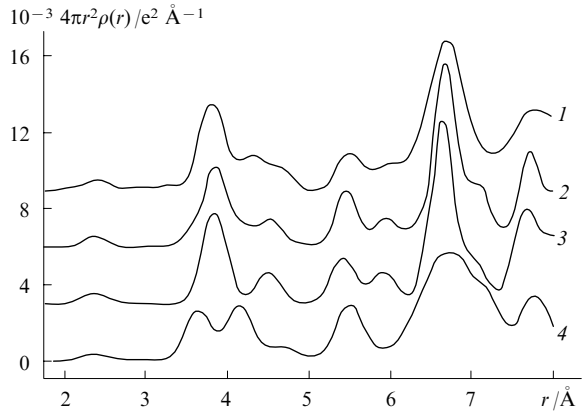


Figure 14. The REDD curve for a $Ce_{0.6}Sm_{0.4}O_{1.8}$ sample calcined at 700 °C (*1*) and the model REDD curves for ($0.2\,Sm_2O_3 + 0.6\,CeO_2$) (*2*), CeO_2 (*3*) and Sm_2O_3 (*4*).

Thus, a conventional X-ray diffraction pattern shows that doping of CeO_2 with Sm^{3+} cations leads to formation of the solid solution with the fluorite structural type and an increased unit cell parameter due to the introduction of the larger cation ($R_{Ce^{4+}} = 0.88$ Å, $R_{Sm^{3+}} = 0.97$ Å). Using the REDD method, it was also shown that the local structure of

Table 2. Theoretical interatomic distances (r) and coordination numbers (CN) for CeO_2 ($a = 5.411$ Å), a perfect solid solution $Ce_{0.6}Sm_{0.4}O_{1.8}$ ($a = 5.445$ Å) and experimental data for a $Ce_{0.6}Sm_{0.4}O_{1.8}$ sample.

Ceria			Perfect solid solution $Ce_{0.6}Sm_{0.4}O_{1.8}$			$Ce_{0.6}Sm_{0.4}O_{1.8}$ sample		
distance	r/Å	CN	distance	r/Å	CN	distance	r, Å	CN
M–O	2.343	8	M–O	2.36	7.2	M–O	2.18	2.0
						M–O	2.42	5.4
M–M	3.826	12	M–M	3.85	12.0	M–M	3.78	10.1
M–O	4.487	24	M–O	4.52	21.6	M–O	4.04	14.0
						M–M	4.34	3.7
						M–O	4.67	11.6
M–M	5.411	6	M–M	5.445	6.0	M–M	5.48	3.8
M–O	5.897	24	M–O	5.93	21.6	M–O	5.97	
M–M	6.627	24	M–M	6.67	24.0	M–M	6.67	26.5
M–O	7.029	32	M–O	7.07	28.8	M–O	7.07	24.0

this solid solution in the region $r = 2-6$ Å is significantly distorted.

Cerium–bismuth oxides. Similar results (formation of a solid solution with distorted local structure) were also obtained upon doping of ceria with Bi^{3+} cations. Samples of the composition $Ce_{1-x}Bi_xO_y$ ($x = 0.1-0.5$) were studied.[92,93] As in the case of samarium, doping of CeO_2 with bismuth leads to formation of single-phase systems, namely, solid solutions with a fluorite-like structure. As the content of bismuth ions increases, the unit cell parameter increases, the size of the coherent scattering region decreases and a structural distortion of the solid solution occurs. As was shown by the REDD method (Table 3), the cerium–bismuth oxides contain no individual oxide clusters Bi_2O_3. The local structure of the solid solutions is characterized by highly disordered cation sublattice, oxygen vacancies and, as a consequence, changed interatomic distances.

Table 3. Interatomic distances and coordination numbers for CeO_2, $Ce_{0.6}Bi_{0.4}O_{1.85}$ solid solution (calculated) and $Ce_{0.6}Bi_{0.4}O_y$ sample (experimental values obtained by the REDD method).

Distance	CeO_2		$Ce_{0.6}Bi_{0.4}O_{1.85}$		$Ce_{0.6}Bi_{0.4}O_y$	
	r/Å	CN	r/Å	CN[a]	r/Å	CN
M–O	2.343	8	2.363	8	2.27	7.0
M–M	3.826	12	3.859	12	3.80	13.09
M–O	4.487	24	4.525	24	4.31	6.3
					4.54	18.0
M–M	5.411	6	5.457	6	5.45	4.53
M–O	5.897	24	5.947	24	5.97	29.3
M–M	6.627	24	6.683	24	6.59	21.9
M–O	7.029	32	7.089	32	6.90	38.2

[a] CeO_2 and the perfect solid solution have the same coordination numbers because both systems belong to the fluorite structural type.

A characteristic feature of the RDA curves obtained by EXAFS is a decrease in the amplitudes of all coordination peaks with an increase in the dopant concentration. Data on the changes in the amplitudes for the Ce–O and Ce–M distances are collected in Table 4. The greatest changes were obtained for the cation sublattice which becomes highly disordered. The REDD curves do not contradict this conclusion. The coordination numbers for the M–M distances in the long-distance coordination spheres decrease. In addition, the M–M distances are shortened by 0.1 Å for the first and third coordination spheres compared to the theoretical data for a perfect solid solution. In addition, the RDA curves obtained from the EXAFS spectra show a significant decrease in the amplitudes of the long-distance peaks with an increase in the content of the dopant cation; this indicates some symmetry violation in the structure.

Table 4. Structural parameters of $Ce_{1-x}Bi_xO_y$ samples determined by EXAFS.[92]

x	Unit cell parameter /Å	Crystallite size /Å	Relative amplitudes of peaks on the EXAFS RDF curves (%)	
			first peak Ce–O	first peak Ce–M
0	5.411	220	100.0	100.0
0.1	5.423	95	99.5	89.3
0.2	5.435	70	93.0	86.0
0.3	5.446	70	–	–
0.4	5.457	70	92.8	67.5
0.5	5.482	80	88.1	65.1

3. Zirconium dioxides

Zirconia-based catalytic systems are promising catalysts and supports for catalysts of redox reactions, organic synthesis, selective oxidation, isomerization of hydrcarbons and complex cleaning of internal combustion engine exhaust gases from carbon oxides and NO_x.[60,94]

The properties of the zirconia-based catalysts are mainly determined by the structural features of the phases formed using various methods for the synthesis of catalysts. Zirconia is prone to polymorphism.[95–99] Stable ZrO_2 phases include a low-temperature monoclinic phase (m) and two high-temperature phases, a tetragonal (t) and a cubic (c) one. They have different bulk and local structures (Fig. 15).

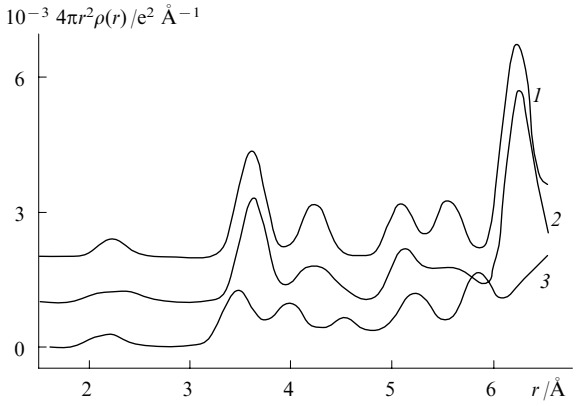


Figure 15. The model REDD curves for the cubic (*1*), tetragonal (*2*) and monoclinic (*3*) phases of ZrO_2.

In addition to the stable ZrO_2 polymorphs, there are metastable[100] cubic (c′) and tetragonal (t′) phases with the stability range from 200 to 800 °C. These phases precede the formation of stable m-ZrO_2 in the course of thermal decomposition of salts and dehydration of zirconium hydroxides. The structures of the metastable phases of zirconium oxide were investigated.[101,102] A study of the oxides prepared by deposition from a zirconyl nitrate solution[35] revealed the formation of amorphous polynuclear hydroxy complexes with the short-range order similar to the order in the cubic ZrO_2. Structural features of these complexes (Fig. 16) include a shortened Zr–Zr distance (by 0.2 Å compared to the Zr–Zr distance in the cubic phase) and the presence of NO_3^- and OH^- groups. Heat treatment at 380°C followed by cooling to room temperature led to the appearance of a monoclinic ZrO_2 phase with a crystallite size of about 60 Å. The amount of this phase depends on the pH value of the precipitation solution and on the content of residual NO_3^- and OH^- groups that stabilize the cubic structure.

Thus, the commonly accepted opinion that the particle size of 300 Å is critical[103,104] to the existence of the monoclinic phase and that smaller particles crystallize as

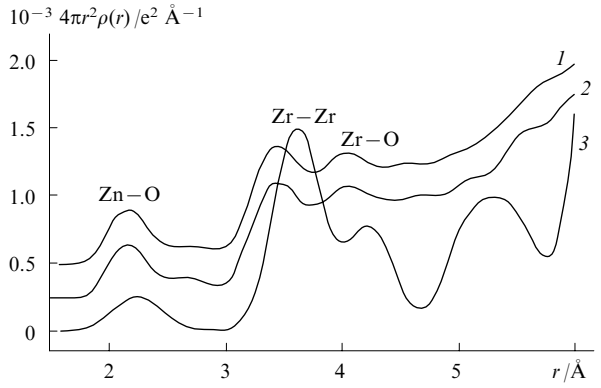


Figure 16. Experimental REDD curves for zirconium oxides synthesized at pH 7 (*1*) and 9 (*2*) and calcined at 110 °C and the model curve for cubic ZrO_2 (*3*).[35]

tetragonal or cubic polymorphs was not confirmed, *viz*., particles of the monoclinic phase observed in the experiments were about 60 Å in size.[34, 35]

a. The structures of modified zirconium oxides

Metastable zirconia phases can be stabilized by doping with anions and cations. In the case of heterovalent isomorphism the valence balance is shifted due to the changes in the anion sublattice (oxygen vacancies appear) [105, 106] or in the cation sublattice (interstitial alloys are formed, interstices are filled with new cations, excess oxygen atoms occupy cation vacancies).[70, 107–109] As for the CeO_2 oxides, non-stoichiometric compounds with the fluorite-type structure with defects (vacancies or inclusions in the cation and anion sublattices) are formed depending on the chemical composition, valence and ionic radius of the dopant cation or anion.

It is highly disordered compounds with well-developed surfaces that are promising for catalytic applications. Modification of zirconia with cations whose valence is lower than that of Zr^{4+} allows one to obtain stable defect structures with improved ionic conductivity. One can also expect an additional improvement of the functional properties of the material upon its transition to the nanostructured state during the synthesis.[110]

Yttrium–zirconium oxides. The formation of yttrium-stabilized zirconia (3.4 mol.% Y_2O_3/ZrO_2) obtained by codeposition of hydroxides followed by drying in a microwave oven and calcination in the temperature range 300–1000 °C was studied.[110–112] According to PXD data, the oxide calcined at 300 °C (ZrO_2-300) is X-ray amorphous. Raising the temperature leads to successive formation of cubic and tetragonal ZrO_2 with an increasing degree of tetragonal distortion characterized by the $c/\sqrt{2a}$ ratio (Table 5). The amount of monoclinic ZrO_2, which is formed at temperatures above 600 °C, was at most 5%.

The structures of the modified oxides ZrO_2-300 and ZrO_2-400 with the highest degree of dispersion were determined by the REDD method. Figure 17 presents the experimental REDD curves and the model curves for the cubic and tetragonal ZrO_2 structures. The REDD curve for the X-ray amorphous ZrO_2-300 sample exhibits peaks only to 4.5 Å, thus indicating a small crystallite size (at most 10 Å in diameter). The short-range atomic order in these particles corresponds to the order in the defect cubic ZrO_2. The

Table 5. X-Ray diffraction characteristics of Y/ZrO_2 samples calcined at different temperatures.

Sample	T_{calc} /°C	Unit cell parameters of t-ZrO_2 phase /Å	$c/\sqrt{2a}$	D (t-ZrO_2 phase) /Å	Content of m-ZrO_2 phase (%)
1	300	–	–	–	–
2	400	a = 3.629, c = 5.106	0.995	100	–
4	600	a = 3.610, c = 5.162	1.011	135	< 2
6	800	a = 3.608, c = 5.166	1.012	220	< 5
8	1000	a = 3.608, c = 5.167	1.013	400	< 5

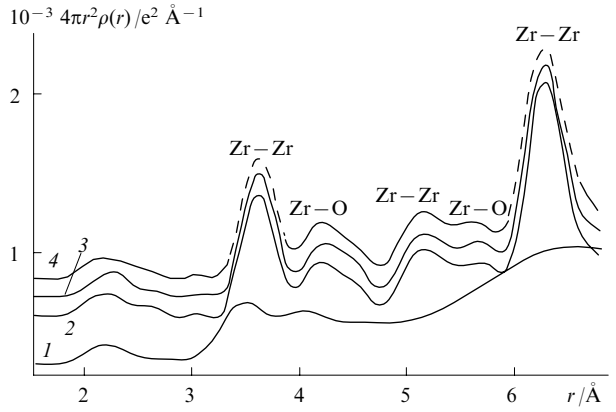


Figure 17. The REDD curves for the ZrO_2-300 (*1*) and ZrO_2-400 (*2*) samples and the model curves for cubic (*3*) and tetragonal (*4*) ZrO_2 structures.

defectiveness manifests itself in shortening of the Zr–Zr distance and in changes in the amplitude ratio of the peaks corresponding to the Zr–O and Zr–Zr distances in the structure of the cubic phase (r = 3.3–4.5 Å).

The oxide ZrO_2-400 also has a defective structure. Although the cation sublattice of ZrO_2-400 remains cubic ($c/\sqrt{2a} \approx 1$), the shape of the Zr–O peak on the REDD curve ($r \approx 2.2$ Å) matches that of the peak for the model tetragonal distortion of the oxygen sublattice. Further increase in the calcination temperature leads to tetragonal distortion of the cation sublattice ($c/\sqrt{2a} > 1$). The tetragonal phase thus formed also has a defective structure and differs from the stable tetragonal ZrO_2 phase obtained at temperatures above 1000 °C (a = 3.64, c = 5.27 Å, $c\sqrt{2a}$ = 1.02) in the unit cell parameters, the degree of tetragonal distortion and the presence of vacancies (owing to Y^{3+} cations).

Thus, the PXD and REDD data suggest that an increase in the calcination temperature is accompanied by the formation of X-ray amorphous complexes with the short-range atomic order similar to the order in the cubic ZrO_2 and followed by the formation of cubic ZrO_2 with tetragonal distortion in the oxygen sublattice only; at 600 °C, tetragonal distortion of the cation sublattice occurs.

Calcination also causes the actual structure of the samples to change. Using the ratio of the particle sizes

obtained from adsorption and X-ray diffraction data, the crystallite coalescence coefficient (ξ) was calculated. The sample calcined at 400 °C is characterized by a negative ξ value, which indicates a well-developed specific surface ($S_{BET} > S_{X\text{-ray}}$) and high porosity of the sample. As the calcination temperature increases, the ξ value increases to 0.43, which corresponds to formation of blocks with numerous interfaces. The existence of intergrain boundaries was confirmed by small-angle X-ray scattering (SAXS)[112] and by high-resolution electronic spectroscopy. An analysis of the SAXS diffraction patterns revealed structural features of the real samples, *viz*., a more dense core and a loose shell. According to local energy-dispersive X-ray microanalysis data, grain boundaries are not due to yttrium segregation on the surface of crystallites. The formation of intergrain boundaries is likely due to high defectiveness of the particles being sintered. This specific structure of the material provides an explanation for the enhanced catalytic activity of ZrO_2 in the model reaction of CO oxidation.[113] It was assumed that high catalytic activity of large particles of modified zirconia is due to specific features of their morphology, namely, defects reaching the surface.

Thus, studies by various methods made it possible to reveal the specific features of formation of metastable zirconium oxide phases on all levels including the atomic level (determination of peculiarities of short-range atomic order), the crystallite level (disclosure of changes in substructural characteristics) and the level of secondary particles (appearance of grain boundaries and nanostructuring).

Iron–zirconium oxides. X-ray amorphous samples of iron–zirconium oxides ($Fe^{3+}:Zr^{4+} = 0.097$) calcined at 110 and 400 °C were studied.[36,55] The following types of Fe^{3+} arrangement in the cubic structure of zirconia were considered:

— non-random distribution of Fe^{3+} cations (formation of Fe_2O_3 clusters);

— formation of a solid solution based on the cubic fluorite structure (no vacancies);

— formation of a solid solution with vacancies in the anion and cation sublattices; and

— formation of a solid solution with vacancies and partial replacement of oxygen anions by OH^- groups.

A comparison of the model and experimental REDD curves showed that the last-mentioned model structure with the general formula $[Zr_{0.907q_M}Fe_{0.093q_M}\square_{1-q_M}]\cdot[O_xOH_y\square_{1-q_O}]_2$, where q_M and q_O are the numbers of vacancies in the cation and anion sublattices, respectively, best describes the structure of the samples. The structural formulas obtained for the samples calcined at 110 and 400 °C using the interatomic distances and areas under the coordination peaks on the experimental REDD curves are as follows: $[Zr_{0.7}Fe_{0.07}\square_{0.23}]O_{0.99}(OH)_{1.01}$ and $[Zr_{0.74}Fe_{0.08}\square_{0.18}]O_{1.23}(OH)_{0.74}\square_{0.03}$, respectively. Thus, it was established that materials in the system Fe–Zr–O are oxide–hydroxide compounds with the short-range order that can be described in terms of distorted fluorite structural type. It was shown that high disordering of the structures in question is due to vacancies in the cation sublattice and partial replacement of oxygen ions by OH^- groups in the anion sublattice. Vacancies in the cation sublattice are responsible for the shortening of Zr–Zr distances by 0.2 Å. Heating of the samples to 400 °C leads to a decrease in the number of cation vacancies and OH^- groups and to the appearance of anion vacancies.

Cerium–zirconium oxides. Solid solutions $Zr_xCe_{1-x}O_2$ as components of catalysts for redox processes have better redox properties and higher thermal stability compared to CeO_2.[113–115]

Two key aspects of structural studies of zirconium–cerium oxides are as follows. First, since the diffusion mobility of oxygen ions in the cubic phase is higher than in the tetragonal phase, exact determination of the phase composition is required. Here, one should take into account that the phase diagrams constructed for coarse-grained materials often change as the particle size decreases. In addition, tetragonal distortions of highly disperse materials due to positions of oxygen atoms in the structure are difficult to detect by conventional X-ray diffraction techniques. Second, metastable nanocomposites are characterized by increased probability of nonuniform distribution of dopant cations (formation of a domain structure). This favours separation of a nanocomposite into stable phases and reduction of the diffusion mobility of oxygen ions with an increase in temperature. Therefore, one should not only exactly determine the phase composition, but also best solve the structural problem, *viz*., establish how cations are distributed in the structure. Usually, this is done by PXD of calcined samples for which the diffraction peaks are narrowed due to coarsening of particles (sintering). However, calcination may lead not only to coarsening of particles, but also to changes in the phase composition. Thus, methods for structure determination of highly disperse modified oxides should not involve heat treatment.

In studies of cerium–zirconium catalysts, the region corresponding to the mixed oxides $Ce_{0.5}Zr_{0.5}O_2$ on the phase diagram of the system CeO_2–ZrO_2 deserves particular attention because these composites exhibit the optimum redox properties.[116] The bulk and local structures of the mixed oxide $Ce_{0.5}Zr_{0.5}O_2$ were investigated and the effect of doping with rare-earth metal cations whose valences are lower than that of cerium was studied.[117,118] Oxides of the compositions $(Gd,Pr)_x(Ce_{0.5}Zr_{0.5})_{1-x}O_y$, where $x = 0, 0.1, 0.2, 0.3$ were synthesized according to Pechini[119] to provide a uniform distribution of cations in the structure of the nanomaterial and calcined at 500 °C. Unmodified ceria prepared analogously was used as a reference sample.

An analysis of the X-ray diffraction patterns showed that all samples under investigation are single-phase and have a cubic fluorite structure. The substructural characteristics [bcc lattice constants, microdistortions ($\Delta d/d$)] determined from the diffraction patterns are listed in Table 6. It

Table 6. Substructural parameters of oxides $M_x(Ce_{0.5}Zr_{0.5})_{1-x}O_y$.

Parameter	CeO_2	$Ce_{0.5}Zr_{0.5}O_2$	$Gd_x(Ce_{0.5}Zr_{0.5})_{1-x}O_y$			$Pr_x(Ce_{0.5}Zr_{0.5})_{1-x}O_y$		
x	—	0	0.1	0.2	0.3	0.1	0.2	0.3
D, Å	75	65	55	45	40	55	40	40
$\Delta d/d$	0	0.003	0.004	0.005	0.007	0.005	0.008	0.009

Table 7. Structural parameters of mixed oxides determined by the FPA method.

Parameter	CeO_2	$Ce_{0.5}Zr_{0.5}O_2$	$Gd_x(Ce_{0.5}Zr_{0.5})_{1-x}O_y$			$Pr_x(Ce_{0.5}Zr_{0.5})_{1-x}O_y$		
x	—	0	0.1	0.2	0.3	0.1	0.2	0.3
Unit cell parameter /Å	5.419	5.284	5.294	5.309	5.331	5.310	5.337	5.355
B /Å^{-2} (M—O)	0	0.42	0.42	0.48	0.36	0.36	0.43	0.45
	0.2	1.5	1.5	1.5	1.5	1.5	1.5	1.5
Occupancy of oxygen positions	1	0.992	0.916 [0.975]	0.907 [0.950]	0.890 [0.925]	0.923 [0.975]	0.897 [0.950]	0.900 [0.925]
R_p	3.70	1.49	2.47	2.21	2.28	2.90	2.94	3.12
R_{wp}	4.61	1.96	3.20	2.83	2.88	3.60	3.73	3.95

Note. Numbers in parentheses are the expected values; R_p and R_{wp} are the reliability factors calculated by summation over all points of the X-ray diffraction pattern: $R_p = \dfrac{\sum_{i=1}^{N} |y_i^{exp} - y_i^{theor}|}{\sum_{i=1}^{N} |y_i^{exp}|} \times 100$, $R_{wp} = \sqrt{\dfrac{\sum_{i=1}^{N} W_i \left[y_i^{exp} - y_i^{theor}\right]^2}{\sum_{i=1}^{N} W_i y_i^{exp^2}}} \times 100$, where y is the intensity and W is the weighting factor.

follows that doping of CeO_2 with zirconium cations is accompanied by changes in the substructural characteristics of the initial oxide, namely, the crystallite size decreases and microdistortions of the crystal lattice appear. Additional modification of the oxide with gadolinium and praseodymium cations leads to further decrease in D and to development of microdistortions. Defect formation is due to different ionic radii of the zirconium and dopant cations. The greatest microdistortions of the crystal lattice were found for the mixed oxides containing the largest (praseodymium) cations. Thus, modification of ceria with metal cations in different (compared to cerium) oxidation states and having larger ionic radii causes disordering of the crystal lattice.

The structural parameters listed in Table 7 were determined by FPA. Structure refinement was made for the cubic fluorite structure. The experimental and theoretical diffraction patterns are very similar, which also follows from the small R-factor values. An analysis of the data of Table 7 showed that the mixed oxides under study represent substitution solid solutions with the cubic fluorite structures and their lattice constants vary in accordance with the radii and content of the dopant cations. In the case of cationic modification, the isotropic thermal factor (B) increases as a consequence of distortions in the cation sublattice. The anion sublattices in these compounds also change. Refinement of the occupation of the regular positions of oxygen atoms revealed some oxygen vacancies (no vacancies were detected in pure ceria). This can be explained by the presence of cations whose valence is lower than that of cerium. However, the observed number of vacancies exceeds the expected values (see Table 7). Vacancies are responsible for higher diffusion conductivity of oxygen ions in the mixed oxides compared to the initial CeO_2.

Additional features of the local structure of mixed oxides were detected by the REDD method.[117,118] The oxides $Ce_{0.5}Zr_{0.5}O_2$ are characterized by tetragonal distortion of the oxygen sublattice only, which manifests itself in splitting of the peaks corresponding to the M—O interatomic distances. This structural feature is not detected by conventional X-ray diffraction methods because of high dispersion of the materials. Studies of complex oxides $M_x(Ce_{0.5}Zr_{0.5})_{1-x}O_y$ revealed splitting of the metal—metal peaks on the REDD curve. Figure 18 presents the REDD curve for the mixed oxide $Ce_{0.35}Zr_{0.35}Pr_{0.3}O_y$ and the model curve calculated for a perfect solid solution. Each distance (r = 5.33, 6.53, 7.54 Å) is split into a shorter and a longer one. The set of interatomic distances thus obtained corresponds to two phases with the fluorite structure and lattice constants of about 5.2 and 5.4 Å. The calculated parameters may be attributed to two mixed oxides with the fluorite structures and different cation compositions. Heterogeneity of the materials (formation of domains of different chemical composition) manifests itself only on the local structural level, whereas the diffraction patterns of the samples exhibit broad (due to dispersion and defectiveness) symmetric peaks whose positions correspond to one solid solution with an average lattice constant of 5.3 Å.

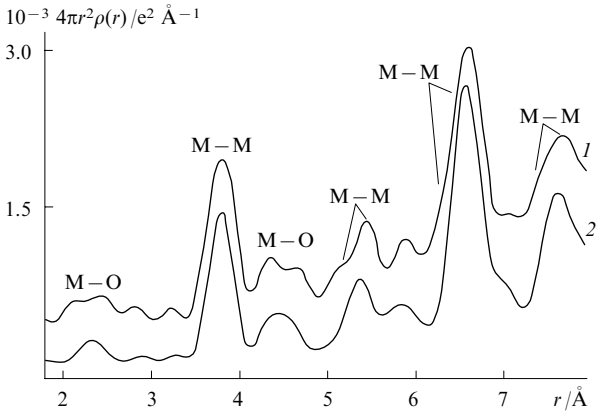


Figure 18. Experimental REDD curve for $Ce_{0.35}Zr_{0.35}Pr_{0.3}O_y$ (*1*) and the model curve for a solid solution with the cubic structure (*2*).[117]

Thus, the REDD studies showed that modification of the oxide $Ce_{0.5}Zr_{0.5}O_2$ with large rare-earth metal cations leads not only to more pronounced structural disordering, but also to the appearance of heterogeneity in the distribution of cations on the local structural level. Segregation occurs and, as a consequence, a domain structure is formed. Heterogeneity of these materials was confirmed in an

EXAFS study.[118] Local heterogeneity leads to segregation of catalysts with an increase in temperature, which imposes limitations on their operating conditions.

b. Supported zirconia

In addition to bulk zirconium oxides, ZrO_2 samples introduced (20 mass %) into the clay structure were studied.[120] The material used as matrix for the zirconium-containing component was montmorillonite, a mineral belonging to finely disperse layered clay-type aluminosilicates. Low degree of crystallization of these minerals is mainly due to disordered arrangement of layers. This is indicated by their diffraction patterns which show only the 00*l* reflections and two-dimensional diffraction bands *hk*0. The structure of montmorillonite is as follows: the aluminosilicate layers comprise alternating chains of interlinked oxygen octahedra and tetrahedra. The interlayer space is filled with water molecules and exchange cations responsible for the changes in the interlayer distance d_{001}. Removal of the exchange cations (water) was followed by introducing the zirconium-containing component into montmorillonite from aqueous solution $ZrOCl_2 \cdot 8\,H_2O$ and calcination of the catalyst at 400 °C.

Clays thus treated are called pillared. The lack of any additional peaks on the diffraction pattern of pillared clay compared to the initial clay may suggest that either the zirconium-containing phase is highly disperse or zirconium ions form a complex embedded into the aluminosilicate structure. From the diffraction pattern it follows that introduction of the zirconium complex causes the interplanar spacing d_{001} in the clay structure to increase from 11.5 to 17.7 Å while the size of the coherent scattering region decreases from 50 to 30 Å. Therefore, one can assume that the zirconium complex is embedded into the interlayer space of the layered clay structure. Using the REDD method, it was shown that the clay structure is changed and the structural parameters of the zirconium complex were determined. To this end, the difference curves of REDD were constructed. Figure 19 shows the REDD curves for the initial and pillared clay and Fig. 20 presents the difference curve of the REDD.

Table 8 lists the interatomic distances and coordination numbers for the intercalated polynuclear complex and the

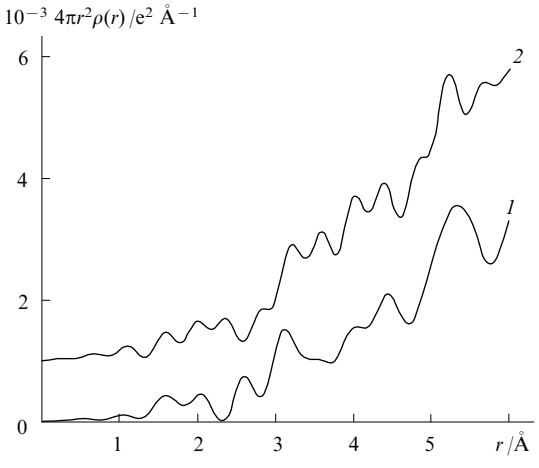


Figure 19. The REDD curves for the initial (*1*) and pillared (*2*) clay.[120]

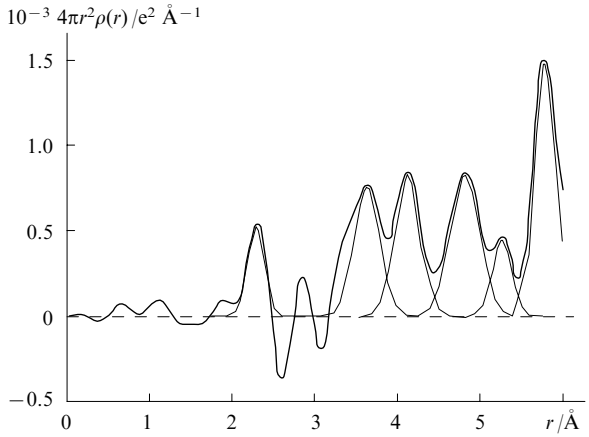


Figure 20. The difference curve of the REDD for pillared clay deconvolved into coordination peaks.[120]

Table 8. Interatomic distances and coordination numbers in the structure of intercalated complex (*1*) and zirconium tetramer (*2*) in the structure of $ZrOCl_2 \cdot 8\,H_2O$.

Parameter	Tetramer			Tetramer – clay	
	Zr – O	Zr – Zr	Zr – Zr	Zr – (Si, Al)	Zr – O
r(*1*) /Å	2.28	3.62	5.26	4.12	4.79
r(*2*) /Å	2.11 – 2.22	3.56	5.03		
CN(*1*)	4.5	2.1	1.0	5.1	9.5
CN(*2*)	8.0	2.0	1.0		

results of calculations for the zirconium tetramer whose structure was determined [121] in a study of different structures formed during the synthesis of zirconium oxide from zirconyl chloride.

Distances in the regions r = 2 – 2.4, 3.6, 4 – 4.2, 4.5 – 4.8, 5.6 – 5.9 Å characteristic of the tetramer $ZrOCl_2 \cdot 8\,H_2O$ were on the difference curve of the REDD. This suggests that the tetrameric complexes are embedded into the initial clay structure. Negative electron density on the difference curve indicates changes in the initial clay structure due to the presence of the zirconium-containing complex. In this case, the distance of 2.6 Å characterizing the interlayer spacing between the networks of tetrahedra increases to 2.8 Å while the distance of 3.1 Å, which characerizes the length of the bond between the cation occupying the octahedral position and the nearest oxygen atom, increases to 3.3 Å. These changes can be due to strain produced upon embedding of the positively charged zirconium tetrameric complex between the layers in the clay structure. In addition, octahedral positions can be filled by zirconium cations having a larger ionic radius compared to the aluminium ion. Tetrameric complexes are arranged in the interlayer space in the regions usually occupied by water molecules or the exchange cation. The lack of additional diffraction peaks on the diffraction pattern of pillared clay suggests that polynuclear particles of the zirconium complex are rather small ($\leqslant$25 – 30 Å for the intra-layer size and $\leqslant$10 Å in the direction perpendicular to the layer). This conclusion was confirmed by high-resolution electron microscopy data.

Thus, a study of the composite material based on zirconia-pillared aluminosilicate clay showed that the zirco-

nium-containing tetrameric complex is embedded between layers of the aluminosilicate structure and forms chemical bonds with the layers.

V. Conclusion

The present review concerning X-ray diffraction structure diagnostics of catalysts and supports for catalysts (typical representatives of nanomaterials) shows that the use of a set of complementary X-ray diffraction methods of investigation allows one to reveal important structural features of these materials, which determine their functional properties.

The development of novel 'tailor-made' methods of investigation and synthesis predetermined the emergence of an interdisciplinary field called nano science and a particular avenue of nanochemistry research.[122] As mentioned above, the REDD method is not a new one; it has been used in structural studies of liquids, gases and alloys. Materials presented in this review show that the use of the REDD method for investigation of nanomaterials required new, more accurate experimental designs as well as new computational procedures and interpretation.

Making use of the REDD method in combination with indirect methods providing structural information (EXAFS, XANES, IR spectroscopy, various electron microscopy techniques, *etc*.)[123, 124] extends our knowledge about relations between the structure and physicochemical properties of nanomaterials and allows one to reveal the reasons for stabilization of nano states.

The author expresses his gratitude to collaborators in the development of the method, Candidates in Chemical Sciences D A Zyuzin and V P Pakharukova as well as to A N Shmakov and K I Shefer, for useful discussions of materials.

The review has been written with the financial support from the Russian Foundation for Basic Research (Project No. 09-03-90424Ukr_f_a).

References

1. X Zhu, R Birringer, U Herr, H Gleiter *Phys. Rev. B* **35** 9085 (1987)
2. A Plançon *Appl. Crystallogr.* **36** 146 (2003)
3. P Scardi, M Leoni, Y H Dong *CPD Newslett.* **24** 23 (2000)
4. L Solovyov *J. Appl. Crystallogr.* **33** 338 (2000)
5. S V Cherepanova, S V Tsybulya *J. Mol. Catal.* **158** 263 (2000)
6. V I Iveronova, G P Revkevich *Teoriya Rasseyaniya Rentgenovskikh Luchei* (The Theory of X-Rays Dispersion) (Moscow: Moscow State University, 1978)
7. K B Aleinikova, E N Zinchenko *Zh. Strukt. Khim.* **50** S100 (2009) [a]
8. E M Moroz *Usp. Khim.* **61** 356 (1992) [*Russ. Chem. Rev.* **61** 188 (1992)]
9. E M Moroz, D A Zyuzin *Z. Kristallogr. Suppl.* (26) 273 (2007)
10. L A Aleshina, A D Fofanov, R N Osaulenko, L A Ligovskaya *Kristallografiya* **50** 428 (2005) [b]
11. L A Aleshina, V P Malinenko, N M Firova, A D Fofanov *Blizhnii Poryadok v Amorfnykh Oksidnykh Plenkakh Tantala i Niobiya* (Short Range Ordering in Amorphous Oxide Films of Tantalum and Niobium, Petrozavodsk, 1977); article deposited in VINITI No. 1557 (1977)
12. T Egami *Local Structure from Diffraction* (New York: Plenum, 1998)
13. S J L Billinge, M G Kanatzidis *Chem. Commun.* 749 (2004)
14. T Egami, S J L Billinge *Structural Analysis of Complex Materials* (Oxford: Pergamon Press, 2003)
15. S J L Billinge *Z. Kristallogr. Suppl.* (26) 17 (2007)
16. R B Neder, V I Korsunskiy *J. Phys. Condens. Matter* **17** 125 (2005)
17. F de Groot, Akio Kotani *Core Level Spectroscopy of Solids* (New York: CRC Press, 2008)
18. D I Kochubei, Yu A Babanov, K I Zamaraev, R V Vedrinskii, V L Kraizman, G N Kulipanov, L N Mazalov, A N Skrinskii, V K Fedorov, B Yu Khel'mer, A T Shuvaev *Rentgenospektral'nyi Metod Izucheniya Struktury Amorfnykh Tel. EXAFS-Spektroskopiya* (X-Ray Method of Investigation of the Structure of Amorphous Bodies. EXAFS Spectroscopy) (Novosibirsk: Nauka, 1988)
19. G V Fetisov *Sinkhrotronnoe Izluchenie. Metody Issledovaniya Struktury Veshchestva* (Synchrotron Radiation. Methods of Investigation of the Structure of Substance) (Moscow: Fizmatlit, 2007)
20. R V Vedrinskii, I I Geguzin *Rentgenovskie Spektry Poglosh-cheniya Tverdykh Tel* (X-Ray Absorption Spectra of Solids) (Moscow: Energoatomizdat, 1991)
21. C T Chantler, S-W Han, G T Seidler, E A Stern, J D Cohen, S Guha, J Yang *J. Appl. Phys.* **92** 801 (2002)
22. A Filipponi *J. Phys. Condens. Matter* **13** R23 (2001)
23. A V Soldatov, T S Ivanchenko, A P Kovtun, S Della Longa, A Bianconi *Phys. Rev. B* **52** 11757 (1995)
24. D I Kochubei, in *EXAFS-spektroskopiya Katalizatorov* (EXAFS Spectroscopy of Catalysts) (Novosibirsk: Nauka, 1992) p. 145
25. E M Moroz, V V Kriventsov, D I Kochubei *Zh. Strukt. Khim.* **50** 1132 (2010) [a]
26. E M Moroz, D A Zyuzin, K I Shefer *Zh. Strukt. Khim.* **48** 269 (2007) [a]
27. E M Moroz, V P Pakharukova, A N Shmakov *Nuclear Instr. Methods Phys. Res. A* **99** 603 (2009)
28. B K Vainshtein, in *Difraktsiya Rentgenovskikh Luchei na Tsepnykh Molekulakh* (X-Ray Diffraction on Chain Molecules) (Moscow: Academy of Sciences of the USSR, 1963) p. 500
29. A F Skryshevskii *Strukturnyi Analiz Zhidkostei i Tverdykh Tel* (Structural Analysis of Liquids and Solids) (Moscow: Vysshaya Shkola, 1980)
30. B L Vainshtein *Dokl. Akad. Nauk SSSR* **112** 640 (1957)
31. P Ratnasamy, A J Léonard *Catal. Rev.* **6** 293 (1972)
32. L B Sorensen, J O Cross, M Newville, B Ravel, J J Rehr, H Stragier, C E Bouldin, J C Woicik, in *Resonant Anomalous X-Ray Scattering: Theory and Applicaations* (Eds G Materlik, C J Sparks, K Fisher) (Amsterdam: North-Holland, 1994) p. 237
33. A N Shmakov, E M Moroz, A L Chuvilin *Nuclear Instr. Methods Phys. Res., A* **405** 470 (1998)
34. D A Zyuzin, E M Moroz, A S Ivanova, A N Shmakov *Kristallografiya* **48** 458 (2003) [b]
35. D A Zyuzin, E M Moroz, A S Ivanova, A N Shmakov, G N Kustova *Kinet. Katal.* **45** 780 (2004) [c]
36. E M Moroz, A S Ivanova, D A Zyuzin *J. Mol. Catal. A: Chem.* **158** 313 (2000)
37. G N Kulipanov, A N Skrinskii *Usp. Fiz. Nauk* **122** 369 (1977) [d]
38. E M Moroz, V A Ushakov, S V Bogdanov, V A Gusev, in *Metody Issledovaniya Kataliticheskikh Sistem 1. Rentgenografiya Katalizatorov* (Methods of Investigation of Catalytic Systems 1. X-Ray Diffraction Analysis of Catalysts) (Novosibirsk: Nauka, 1977) p. 117
39. E M Moroz, S V Bogdanov, N E Buyanova, O A Kovrizhina *Kinet. Katal.* **19** 1029 (1978) [c]
40. E M Moroz, A A Tripol'skii, Yu A Ryndin, B N Kuznetsov *Kinet. Katal.* **18** 1531 (1977) [c]

41. P E Kolosov E M Moroz, A N Startsev, M D Smolikov, N B Shitova, A S Belyi, T P Sorokina, V P Doronik *Kinet. Katal.* **36** 342 (1995) [c]
42. M D Smolikov, A S Belyi, A I Nizovskii, I E Smirnova, A S Semikolenov, V K Duplyakin *React. Kinet. Catal. Lett.* **37** 437 (1988)
43. A S Belyi, M D Smolikov, N M Ostrovskii, Yu M Kolomytsev, V K Dyplyakin *React. Kinet. Catal. Lett.* **37** 457 (1988)
44. P E Kolosov, E M Moroz *Kinet. Katal.* **33** 435 (1992) [c]
45. P E Kolosov E M Moroz *Kinet. Katal.* **36** 337 (1995) [c]
46. Yu G Poltavtsev *Struktura Poluprovodnikovykh Rasplavov* (The Structure of Semiconductor Melts) (Moscow: Metallurgiya, 1984)
47. E M Moroz, K I Shefer, D A Zyuzin, A S Ivanova, E V Kulko, V V Molchanov *React. Kinet. Catal. Lett.* **87** 367 (2006)
48. K I Shefer, D A Zyuzin, E M Moroz *Izv. Akad. Nauk, Ser. Fiz.* **70** 1068 (2006) [e]
49. N N Kiseleva, V A Dudarev, V S Zemskov *Usp. Khim.* **79** 162 (2010) [*Russ. Chem. Rev.* **79** 145 (2010)]
50. *Pearson's Handbook of Crystallographic Data for Intermetallic Phases* (Metals Park, OH: American Society for Metals, 1989)
51. S V Tsybulya, S V Cherepanova, L P Solov'eva *Zh. Strukt. Khim.* **37** 379 (1996) [a]
52. G Paglia, E S BozPin, S J L Billinge *Chem. Mater.* **18** 3242 (2006)
53. K I Shefer, E M Moroz, L I Isupova, I V Kharina, Yu Yu Tanashev *Z. Kristallogr. Suppl.* (26) 279 (2007)
54. A S Ivanova, E M Moroz, M A Fedotov, G S Litvak *Neorg. Mater.* **36** 440 (2000) [f]
55. D A Zyuzin, E M Moroz, A S Ivanova, V I Zaikovskii *Neorg. Mater.* **36** 447 (2000) [f]
56. Yu V Frolova, D I Kochubey, V V Kriventsov, E M Moroz, S Neofitides, V A Sadykov, D A Zyuzin *Nuclear Instr. Methods Phys. Res. A* **543** 127 (2005)
57. V P Pakharukova, E M Moroz, D A Zyuzin *Zh. Strukt. Khim.* **51** 288 (2010) [a]
58. B E Warren, R L Mozzi *J. Appl. Crystallogr.* **8** 674 (1975)
59. A B Stiles *Catalyst Supports and Supported Catalysts: Theoretical and Applied Concepts* (Stoneham, MA: Butterworth, 1987)
60. *Physical and Chemical Aspects of Adsorbents and Catalysts* (Ed. B Linsen) (London: Academic Press, 1970)
61. V A Ushakov, E M Moroz, E A Levitskii *Kinet. Katal.* **26** 1200 (1985) [a]
62. V A Ushakov, E M Moroz *Kinet. Katal.* **26** 968 (1985) [a]
63. K C Hass, W F Schneider, A Curioni, W Andreoni *Science* **282** 265 (1998)
64. S V Tsybulya, G N Kryukova *Phys. Rev. B* **77** 024112 (2008)
65. S V Tsybulya, Doctoral Thesis in Physical and Mathematic Sciences, Institute of Inorganic Chemistry, Siberian Branch of the Russian Academy of Sciences, Novosibirsk, 2004
66. E M Moroz, D A Zyuzin, K I Shefer, L A Isupova *Zh. Strukt. Khim.* **48** 753 (2007) [a]
67. E A Kummerle, G Heger *J. Solid State Chem.* **147** 485 (1999)
68. O T Surensen *J. Solid State Chem.* **18** 217 (1976)
69. C H B Steele, J M Floyd *Proc. Br. Ceram. Soc.* **19** 55 (1971)
70. J Faber Jr, M A Seitz, M H Mueller *J. Phys. Chem. Solids* **37** 903 (1976)
71. Y M Chiang, E B Lavik, I Kosacki, H L Tuller *J. Electroceram.* **1** 7 (1997)
72. X T Sayle, S C Parker, C R A Catlow *Surf. Sci.* **316** 329 (1994)
73. V Shapovalov, H Metiu *J. Catal.* **245** 205 (2007)
74. P V Snytnikov, V V Galvita, V D Belyaev, G L Semin, A I Stadnichenko, V A Sobianin, in *Proceedings of the International Conferens Evropacat-VI, Innsbruck, Austria, 2003* p. 333
75. G Avgouropoulos, Th Ioannides, H Matralis, J Batista *Catal. Lett.* **73** 33 (2001)
76. G Avgouropoulos, Th Ioannides *Appl. Catal. A* **244** 155 (2003)
77. P Ratnasamy, D Srinivas, C V V Satyanarayana, P Manikandan, R S S Kumaran, M Sachin, V N Shetti *J. Catal.* **221** 455 (2004)
78. V A Sadykov, Yu V Borkhert, G A Alikina, A I Lukashevich, N V Mezentseva, V S Muzykantov, E M Moroz, V A Rogov, V I Zaikovskii, D A Zyuzin, N F Uvarov, A V Ishchenko, V V Zyryanov, A Smirnov *Fiz. Khim. Stekla* **33** 456 (2007) [g]
79. A V Gural'skii, G R Kosmambetova, V I Gritsenko, P E Strizhak, V P Kol'ko, E M Moroz, R V Gulyaev, A I Boronin, T S Ivashchenko, in *Nanosistemy, Nanomaterialy, Nanotekhnologii (Sbornik Nauchnykh Trudov)* [Nanosystems, Nanomaterials, Nanotechnologies (The Collection of Proceedings)] (Kiev: Institute of Metallophysics National Academy of Sciences, Ukraine, 2009) Vol. 7, p. 185
80. D-J Kim *J. Am. Ceram. Soc.* **72** 1415 (1989)
81. V P Kol'ko, E M Moroz, V V Kriventsov, D A Zyuzin *Izv. Akad. Nauk, Ser. Fiz.* **71** 718 (2007) [e]
82. V A Sadykov, T G Kuznetsova, G M Alikina, Yu V Frolova, A I Lukashevich, V S Muzykantov, V A Rogov, L Ch Batuev, V V Kriventsov, D I Kochubey, E M Moroz, D A Zyuzin, E A Paukshtis, E B Burgina, S N Trukhan, V P Ivanov, L G Pinaeva, Yu A Ivanova, V G Kostrovskii, S Neophytides, E Kemnitz, K Scheurel, C Mirodatos, in *New Topics in Catalysis Research* (Ed. D McReynolds) (New York: Nova Sci. Publ., 2006) p. 97
83. E Mamontov, T Egami *J. Phys. Chem. Solids* **61** 1345 (2000)
84. M Yashima, S Kobayashi, T Yasui *Solid State Ionics* **177** 211 (2006)
85. A Trovarelli, in *Catalysis by Ceria and Related Materials* (London: Imperial College Press, 2002) p. 528
86. G R Kosmambetova, P E Strizhak, E M Moroz, A V Gural'skii, V P Kol'ko (Pakharukova), V I Gritsenko *Katal. Prom.* (2) 13 (2008) [h]
87. Russ. P. 2377054; *Byull. Izobret.* (36) (2009)
88. M Sugiura *Catal. Surv. Asia* **7** 77 (2003)
89. D A Zyuzin, E M Moroz, V A Sadykov, T G Kuznetsova, A N Shmakov *Izv. Akad. Nauk, Ser. Fiz.* **68** 728 (2004) [e]
90. Yu A Pyatenko *Zh. Strukt. Khim.* **4** 708 (1963) [a]
91. Yu A Pyatenko *Izv. Akad. Nauk SSSR, Neorg. Mater.* **7** 630 (1971) [f]
92. S Dikmen, P Shuk, M Greenblatt *Solid State Ionics* **112** 299 (1998)
93. V A Sadykov, T G Kuznetsova, V P Doronin, E M Moroz, D A Zyuzin, D I Kochubei, B N Novgorodov, V N Kolomiichuk, G M Alikina, R V Bunina *Top. Catal.* **32** 29 (2005)
94. V A Sadykov, G Kuznetsova, G M Alikina, Yu V Frolova, A I Lukashevich, Yu V Potapova, V S Muzykantov, V A Rogov, V V Kriventsov, D I Kochubei, E M Moroz, D A Zyuzin, V I Zaikovskii, V N Kolomiichuk, E A Paukshtis, E B Burgina, V V Zyryanov, N F Uvarov, S Neophytides, E Kemnitz *Catal. Today* **93** 45 (2004)
95. P Afanasiev, A Thiollier, M Breysse, J L Dubois *Top. Catal.* **8** 147 (1999)
96. S T Buljan, H A McKinstry, V S Stubican *J. Am. Ceram. Soc.* **59** 351 (1976)
97. N T McDevitt, D L Baun *J. Am. Ceram. Soc.* **47** 622 (1964)
98. V B Glushkova *Polimorfizm v Okisnykh Sistemakh $La_2O_3-ZrO_2$ i $La_2O_3-HfO_2$. Redkozemel'nye Metally, Splavy i Soedineniya* (Polymorphism in Oxide Systems $La_2O_3-ZrO_2$. Rare-earth Metals, Alloys and Compounds) (Moscow: Nauka, 1973)
99. Y Murase, E Kato, H Matsumoto *J. Chem. Jpn.* 2329 (1972)

100. V N Strekalovskii, Yu N Polezhaev, S F Pal'guev *Oksidy s Primesnoi Razuporyadochennost'yu. Sostav, Struktura, Fazovye Prevrashcheniya* (Oxides with Impurity Disorder. Composition, Structure, Phase Transformations) (Moscow: Nauka, 1987)
101. E M Moroz, in *II Mezhdunarodnaya Nauchnaya Konferentsiya 'Nanostrukturnye Materialy-2010: Belarus' – Rossiya – Ukraina' (Tezisy Dokladov)* [The IInd International Conference 'Nanostructure Materials-2010: Belarus – Russia – Ukraine' (Abstracts of Reports), Kiev, 2010] p. 245
102. N Igawa, I Yoshinobu, I-W Chen *J. Am. Ceram. Soc.* **84** 1169 (2001)
103. B Ya Sukharevskii, B G Alapin, A M Gavrish *Dokl. Akad. Nauk SSSR* **156** 677 (1964) [i]
104. J-D Lin, J-G Duh *J. Mat. Sci.* **32** 5779 (1964)
105. R Collongues *La Non-stoechiométrie* (Paris: Masson, 1971)
106. V P Gorelov, S V Pal'guev *Izv. Akad. Nauk, SSSR, Neorg. Mater.* **13** 181 (1977) [f]
107. S K Filatov, V A Frank-Kamenetskii *Kristallografiya* **14** 505 (1969) [b]
108. P Fornasiero, R Di Monte, G R Rao, J Kaspar, S Meriani, A Trovarelli, M Graziani *J. Catal.* **151** 168 (1995)
109. N N Bulgakov, V A Sadykov, V V Lunin, E Kemnitz *React. Kinet. Catal. Lett.* **76** 103 (2002)
110. G R Kosmambetova, P E Strizhak, E M Moroz, T E Konstantinova, A V Gural'skii, V P Kol'ko, V I Gritsenko, I A Danilenko, O A Gorban' *Teor. Eksp. Khim.* **43** 96 (2007) [j]
111. P E Strizhak, A I Tripol'skii, T N Gurnik, F V Tuzikov, E M Moroz, T E Konstantinova, N A Tuzikova, V P Kol'ko (Pakharukova), I A Danilenko, O A Gorban' *Teor. Eksp. Khim.* **44** 138 (2008) [j]
112. V P Pakharukova, E M Moroz, V V Kriventsov, D A Zyuzin, G R Kosmambetova, P E Strizhak *Appl. Catal. A* **365** 159 (2009)
113. P Fornasiero, G Balducci, R Di Monte, J Kašpar, V Sergo, G Gubitosa, A Ferrero, M Graziani *J. Catal.* **164** 173 (1996)
114. G R Kosmambetova, V I Gritsenko, P E Strizhak, A M Korduban *Teor. Eksp. Khim.* **42** 119 (2006) [j]
115. A Trovarelli *Catal. Rev. Sci. Eng.* **38** 439 (1996)
116. G Colón, F Valdivieso, M Pijolat, R T Baker, J J Calvino, S Bernal *Catal. Today* **50** 271 (1999)
117. V P Kol'ko (Pakharukova), D A Zyuzin, V A Sadykov, V V Kriventsov, E M Moroz *Fiz. Khim. Stekla* **33** 470 (2007) [g]
118. V P Kolko (Pakharukova), V V Kriventsov, D I Kochubey, D A Zyuzin, E M Moroz, V A Sadykov, G R Kosmambetova, P Y Strizhak *Nuclear Instr. Methods Phys. Res. A* **575** 91 (2007)
119. US P. 3300697 (1967)
120. D A Zyuzin, E M Moroz, T G Kuznetsova, V A Sadykov, V P Doronin *React. Kinet. Catal. Lett.* **81** 137 (2004)
121. G M Muha, P A Vaughan *J. Chem. Phys.* **33** 194 (1960)
122. G B Sergeev *Nanokhimiya* (Nanochemistry) (Moscow: Moscow State University, 2007)
123. B Sksrman, D Grandjean, R E Benfield, A Hinz, A Andersson, L R Wallenberg *J. Catal.* **211** 119 (2002)
124. A I Gusev *Nanomaterialy, Nanostruktury, Nanotekhnologii* (Nanomaterials, Nanostructures, Nanotechnologies) (Moscow: Fizmatlit, 2009)

[a] — *J. Struct. Chem. (Engl. Transl.)*
[b] — *Crystallogr. Rep. (Engl. Transl.)*
[c] — *Kinet. Catal. (Engl. Transl.)*
[d] — *Physics-Uspekhi (Engl. Transl.)*
[e] — *Bull. Russ. Acad. Sci., Phys. (Engl. Transl.)*
[f] — *Inorg. Mater. (Engl. Transl.)*
[g] — *Glass Phys. Chem. (Engl. Transl.)*
[h] — *Catal. Ind. (Engl. Transl.)*
[i] — *Dokl. Phys. (Engl. Transl.)*
[j] — *Theor. Exp. Chem. (Engl. Transl.)*